Energy & Environmental Science

ROYAL SOCIETY OF CHEMISTRY

PAPER

View Article Online
View Journal | View Issue

Cite this: *Energy Environ. Sci.*, 2025, **18**, 3852

Spontaneous passivation of selective Zn(101) plating *via* dangling bond saturation and electrostatic interaction regulation for high-utilization, fast-kinetics zinc anodes†

Yuxuan Zhang,[a] Minyoung Kim,[a] Dong Hun Lee,[a] Fei Qin,[a] Han-Wook Song,[b] Chung Soo Kim,[c] Jeongmin Park,[cd] Chohee Kim,[ce] Fang Lian[f] and Sunghwan Lee*[a]

Received 21st November 2024,
Accepted 18th February 2025

DOI: 10.1039/d4ee05498a

rsc.li/ees

Although Zn(101) exhibits faster Zn^{2+} plating/stripping kinetics and stronger bonding with Zn^{2+} compared to Zn(002), the application of Zn(101) in Zn batteries has been limited due to its higher reactivity with water. However, a novel approach utilizing spontaneous self-passivation of plated Zn(101) offers the potential to harness its favorable kinetics and stronger Zn–Zn bonding for battery applications. Here, we present a high-utilization and fast-kinetics Zn anode by promoting selective (101) facet growth and achieving spontaneous passivation of the underlying Zn plating. A non-stoichiometric Sn–O system is selected as the modification material because of its ability to engineer crystal structures (amorphous, rutile, and layered) and manipulate electrical polarity (n-type *vs.* p-type). The optimized p-type $SnO_{1.17}$ saturates dangling bonds of Zn(101), benefiting the preferential growth of well-aligned Zn(101) planes. Besides, the Zn^{2+} plating location is altered underlying the interphase due to synergetic effects of lower Zn^{2+} migration barriers of the layered structure and electron-blocking properties of $SnO_{1.17}$. Consequently, a high Zn utilization ratio of over 91.5% is achieved in 800 hours, with an impressively low overpotential of 43 mV. Furthermore, an anode-free system combining a $ZnMn_2O_4$ cathode and a $SnO_{1.17}$@Cu anode retained 81.6% capacity after 200 cycles.

Broader context

Inducing (002)-oriented Zn^{2+} plating has been widely explored as an effective strategy for achieving reversible Zn^{2+} plating/stripping, largely due to its resistance to water-triggered parasitic reactions. However, the weak bonding between Zn^{2+} and the Zn(002) plane often leads to lattice distortion at high Zn plating amounts. Furthermore, the slower mass transfer at Zn(002) can result in sluggish Zn^{2+} plating/stripping kinetics. In contrast, the Zn(101) plane offers faster mass transfer kinetics and stronger Zn^{2+} bonding; yet, its high reactivity towards water has limited its application. To leverage the advantages of Zn(101) while maintaining electrochemical stability, we constructed a $SnO_{1.17}$ interphase on the anode. This interphase guided Zn^{2+} plating beneath its structure with a regulated (101) orientation, effectively isolating the (101)-oriented Zn from water molecules and eliminating water-triggered parasitic reactions. The $SnO_{1.17}$ interphase further facilitates rapid Zn^{2+} transfer and provides low polarization, reducing voltage hysteresis during cycling. Additionally, the stronger interaction between Zn^{2+} and the Zn (101) plane prevents lattice distortion even at high Zn plating amounts, resulting in well-aligned Zn(101) planes. This study underscores the potential of oriented Zn^{2+} plating along the (101) facet to achieve a high Zn utilization ratio and superior Zn anode kinetics.

Introduction

Zn ion batteries (ZIBs) with mild aqueous electrolytes (*i.e.*, $ZnSO_4$) have been considered grid-level energy storage solutions due to their high theoretical capacity (820 mA h g^{-1}), resource abundance, and eco-friendliness.[1–3]

However, the uncontrollable Zn dendrite growth, hydrogen evolution reaction (HER), and corrosion severely limit the

[a] *School of Engineering Technology, Purdue University, West Lafayette, IN 47907, USA. E-mail: sunghlee@purdue.edu*
[b] *Convergence Research Center for Meta-Touch, Korea Research Institute of Standards and Science (KRISS), Daejeon, Republic of Korea*
[c] *Analysis and Standards Center, Korea Institute of Ceramic and Technology, Jinju, 52851, Republic of Korea*
[d] *Graduate School of Semiconductor Materials and Devices Engineering, Ulsan National Institute of Science and Technology, Ulsan, 44919, Republic of Korea*
[e] *Department of Materials Science and Engineering, Pusan National University, Pusan, 43241, Republic of Korea*
[f] *School of Materials Science and Engineering, University of Science and Technology Beijing, Beijing, 100083, P. R. China*
† Electronic supplementary information (ESI) available. See DOI: https://doi.org/10.1039/d4ee05498a

reversibility and lifespan of ZIBs.[4,5] These issues are more detrimental to practical ZIBs, which require a negative/positive (N/P) capacity ratio lower than 1.08 (referenced to the commercialized lithium-ion batteries, LIBs).[6,7] A Zn utilization ratio (ZUR) higher than 80% is the prerequisite to realize this low N/P ratio.[8] The low ZUR and poor reversibility significantly undermine the advantages of ZIBs compared to alternative technologies such as lithium-ion and sodium-ion batteries. The characteristics of plated Zn, which are normally dominated by the crystallographic (002), (100), and (101) facets of hexagonal close-packed Zn, are highly correlated to the Zn stripping/plating behaviors and concomitant side reactions.[9–11] According to the Gibbs–Curie–Wulff theorem, the (002) facet of Zn metal has a lower reactivity towards water and a slower growth rate due to the lower surface energy compared to that of the (001) and (101) facets.[12,13] Therefore, attention has been focused on inducing the crystalline orientation of plated Zn along the (002) plane, which may reduce dendritic growth, HER, and corrosion.[14–16] Archer *et al.* employed graphene as the anode to induce the (002) oriented growth of Zn^{2+} plating, leading to enhanced Zn^{2+} stripping/plating reversibility.[17] Subsequently, a series of materials such as metallic sulfides, MXenes, and metal–organic frameworks followed the work to modulate the orientation of plated Zn along the (002) facet, which suppressed the formation of dendrites to some extent.[18–20] In addition to the anode modifications, separator alterations (*e.g.*, by sulfonic cellulose coating) and the adoption of electrolyte additives (*e.g.*, anionic surfactants) have also been demonstrated to regulate Zn^{2+} plating along the (002) facet.[21,22]

Despite the effect being somewhat demonstrated, the slower growth rate of Zn(002) compared to Zn(100) and (101) results in a larger polarization during Zn stripping/plating, which negatively impacts battery performance.[23–25] In addition, as research into Zn(002) has progressed, it has been verified that the plated Zn orientation easily deviates from the intended (002) facet, resulting in significant lattice distortion and irreversible Zn^{2+} plating/stripping, due to the weak bonding between the (002) facet and the plated Zn atoms, further compromising structural integrity and efficiency.[9,26] It is urgent to establish an alternative solution to achieve a high ZUR and kinetically favorable Zn^{2+} plating/stripping process.

Although vulnerable to HER and corrosion reactions, Zn(101) has garnered increasing attention from researchers due to its faster growth rates compared to other major facets and stronger Zn–Zn bonding to maintain the desired facet, which shows feasibility to address issues associated with Zn(002). For example, Liu *et al.* demonstrated that the epitaxial growth of the Zn(101) facet can be achieved by constructing a highly oriented Zn(101) substrate, resulting in exceptional Zn^{2+} plating kinetics.[24] Electrolyte additives such as theophylline and dextrin have also been shown to promote the preferential growth of the Zn(101) facet, where the additives are selectively adsorbed onto Zn(002) and Zn(100) facets, directing Zn^{2+} to migrate to and deposit along the (101) facet.[25,27] However, in these studies, the plated Zn(101) is directly exposed to water molecules, leading to inevitable HERs, corrosion reactions, and dendrite growth—issues that will be drastically exaggerated with increased Zn^{2+} plating/stripping amounts. Consequently, the ZUR is critically limited to below 40%, compromising reversibility and energy density.[24,25,27–29]

The primary goal of this study is to harness the favorable kinetics and stronger Zn–Zn bonding strength of Zn(101) towards sustainable Zn anode applications, particularly featuring a high ZUR ($>80\%$). To this end, the following hypotheses were established: (a) selective Zn orientation (in this study (101)) may be achieved by saturating the Zn dangling bonds of the selected (101) facet of Zn. (b) The highly reactive Zn(101) can be spontaneously passivated by an artificial interphase that can shield Zn^{2+} from electrons and rapidly transport Zn^{2+} throughout the interphase. (c) The formation of Zn dendrites can be restricted by an artificial interphase with a high Young's modulus (>100 GPa).

These hypotheses were formulated from the well-known facts that (1) the existence of dangling bonds is directly associated with surface energy, which raises the nucleation energy barrier and consequently limits the growth of crystalline phases;[12,30] (2) the Zn^{2+} plating location is governed by Zn^{2+} diffusion and electron reduction. The rapid diffusion of Zn^{2+}, coupled with limited electron availability within the material, may prevent the reduction of Zn^{2+} upon coming into contact with the interphase. This allows Zn^{2+} to migrate through the interphase until the ions reach its end, where Zn begins plating beneath the interphase upon encountering an electron source (*i.e.*, Zn electrode), immediately being isolated from water/electrolyte;[31,32] and (3) Zn dendrites, whose Young's modulus is as high as $\sim$100 GPa, have been reported to penetrate the artificial interphase of low mechanical strength and cause an internal short circuit.[17,33] Therefore, the mechanical properties of the implemented artificial interphases need to be greater than those of Zn dendrites.

To identify optimal materials for constructing an artificial interphase for the Zn anode, the candidate materials were divided into five main categories: carbon composites, polymers, metal alloys, fluoride materials, and oxide materials, as presented in Fig. 1(a). Among these, carbon composites, metal alloys, and oxide materials demonstrated Young's modulus higher than 100 GPa, which is crucial for inhibiting Zn dendrite formation and thereby preventing battery short circuits. The selected interphase material must also possess electron shielding capabilities, making metal alloys and carbon composites unsuitable due to their electron-conducting nature. Both dielectric and p-type oxide materials meet the electron shielding criterion, creating an electron transfer barrier with the Zn electrode. However, p-type oxide materials may present a distinct advantage over dielectric materials due to their tunable doping and hence the work function energy level to tune the barrier height.[34,35] The tunable barrier height may be of significant advantage for long term sustainability of batteries since dynamic changes in the barrier height (E_b) promote reversible charge (with reduced E_b) and discharge (with increased E_b) processes, which decrease the Zn^{2+} concentration polarization and benefit uniform Zn^{2+} stripping/plating.[36,37]

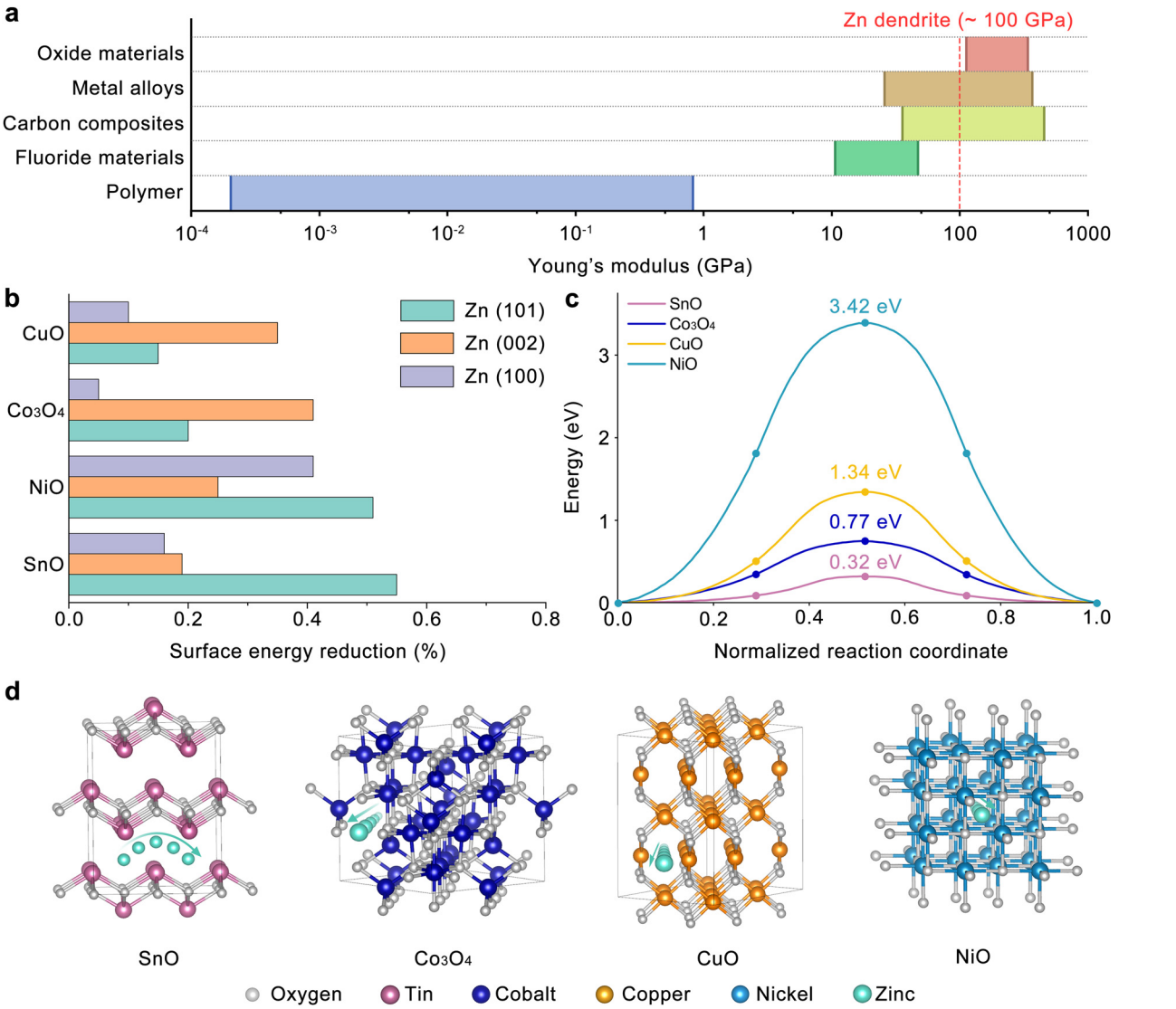

Fig. 1 (a) Overview of Young's moduli of oxide materials, metal alloys, carbon composites, fluoride materials, and polymers. (b) Surface energy variation of Zn(002), (100), and (101) applied with different oxide interphases. (c) Migration energy barrier and (d) the corresponding paths of Zn^{2+} in different oxide materials.

Based on these selection criteria, we narrowed our options to p-type metal oxides such as CuO, NiO, SnO, and Co_3O_4 for further evaluation, specifically focusing on their capabilities to selectively saturate dangling bonds at the Zn(101) surface and promote Zn^{2+} transfer kinetics. According to the calculation results in Fig. 1(b), the surface energy of Zn(101) can be most selectively reduced with SnO, while NiO non-selectively reduces the surface energy of both Zn(101) and (100). The surface energy reduction capability of these p-type oxides was estimated by the overlaps of the projected density of states (pDOS) between the Zn 4s orbital of the Zn facet and O 2p orbital of the oxide. The pDOS calculations are presented in Fig. S1 (ESI†) as a function of Zn orientation and p-type oxide, where the higher overlap of O 2p and Zn 4s orbitals indicates the stronger interactions between the O and Zn dangling bonds, leading to their saturation. The selective reduction in the surface energy of the Zn(101) facet by the implementation of SnO is attributed to these stronger interactions between O and Zn (orbital overlaps) estimated in Fig. S1a (ESI†), resulting in the saturation of Zn dangling bonds.

Furthermore, taking the Zn^{2+} transfer kinetics into consideration, SnO, whose layered structure favors Zn^{2+} transport with the lowest migration energy (~0.32 eV), compared to Co_3O_4, CuO and NiO where Zn^{2+} transfer is limited with much higher migration energies (0.77–3.42 eV), is selected as the ideal candidate for the artificial interphase in the current Zn battery study as shown in Fig. 1(c) and (d).

Herein, we demonstrate reversible Zn^{2+} plating along (101) orientation beneath the $SnO_{1.17}$ interphase by precisely controlling the O ratio in the Sn–O system, which selectively saturates the dangling bonds of Zn(101) and ensures built-in electrostatic interactions and low Zn^{2+} migration barrier.

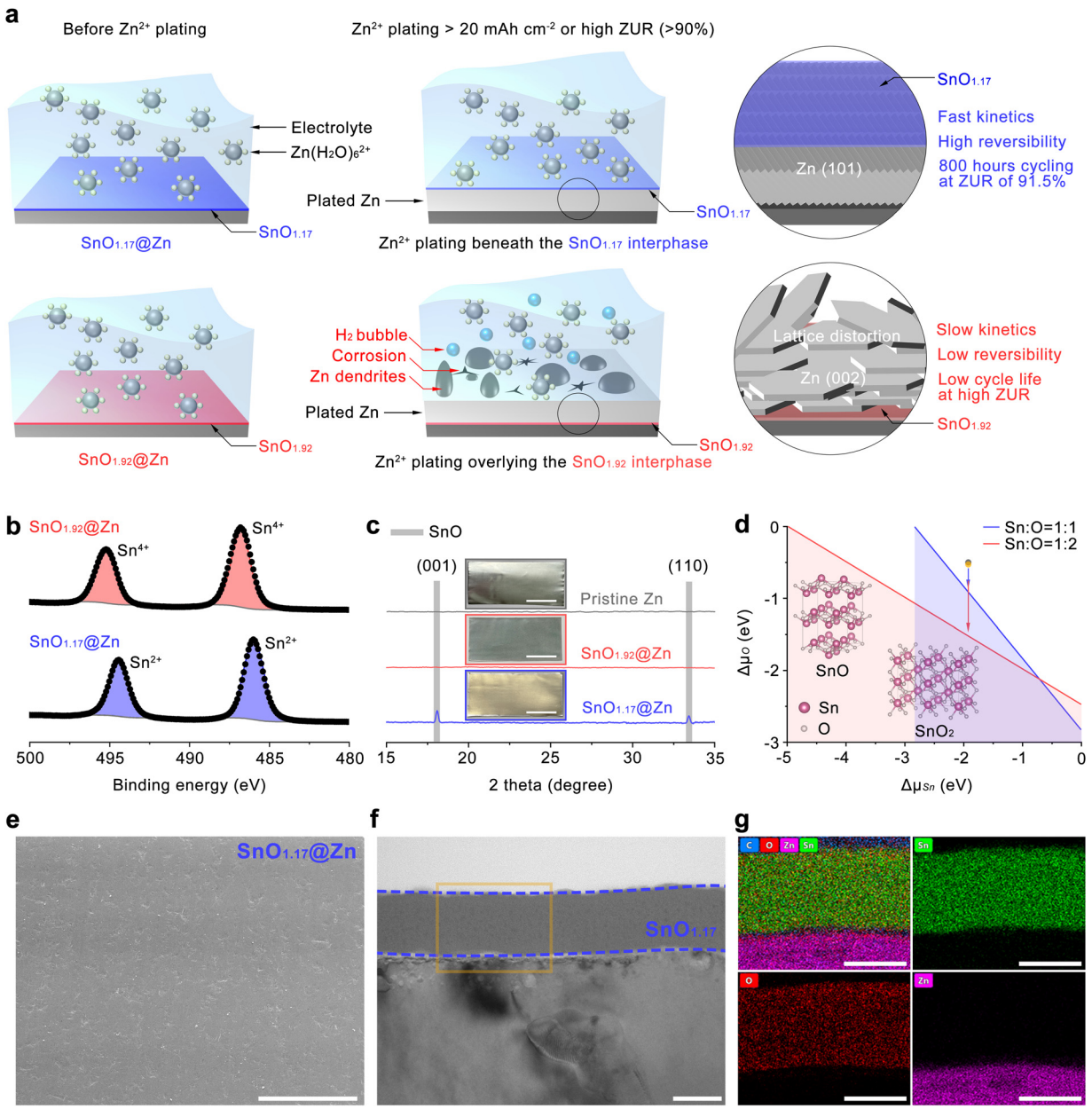

Fig. 2 Mechanism of the two different Zn^{2+} plating behaviors and properties of $SnO_{1.17}$@Zn. (a) Schematic illustration of the underlying Zn(101) plating and overlying Zn(002) plating relative to the interphase. (b) HR-XPS of Sn 3d for $SnO_{1.92}$@Zn and $SnO_{1.17}$@Zn. (c) XRD patterns of pristine Zn, $SnO_{1.92}$@Zn, and $SnO_{1.17}$@Zn with insets showing digital photos of the specimens (scale bar, 4 cm). (d) The chemical potential of Sn and O for crystalline SnO and SnO_2 with insets showing the crystalline atomic structures of the two Sn–O phases. (e) A plane-view SEM image of $SnO_{1.17}$@Zn (scale bar, 100 μm). TEM images of (f) a cross-sectional view and (g) the corresponding elemental mapping micrographs of $SnO_{1.17}$@Zn (scale bar, 50 nm).

Consequently, the preferential growth of the well-aligned Zn(101) facets is facilitated due to the decreased surface energy of Zn(101). Different from the previously reported Zn(101) facet exposed to water, it should be noted that our study first demonstrates simultaneous passivation of the selectively grown Zn(101) facet, preventing direct contacts between the plated Zn(101) and water molecules since Zn(101) is plated underlying the $SnO_{1.17}$ interphase, as shown in Fig. 2(a). The higher growth rate of the (101) facet promotes faster mass transfer, leading to a lower overpotential in the Zn^{2+} plating/stripping process compared to that of the (002) facet.[10,23] In addition, the manipulated Zn^{2+} plating beneath $SnO_{1.17}$ spontaneously eliminates the HER and corrosion by isolating the highly reactive Zn(101) from water, which enables sustainable Zn^{2+} plating/stripping, therefore ensuring superior reversibility under high current density and high ZUR conditions. The $SnO_{1.17}$ interphase characterization and the comparison with $SnO_{1.92}$ validate our hypotheses, which helps to develop an engineering approach to achieve enhanced reversibility and kinetics for Zn anode applications. The Zn anode modified with the $SnO_{1.17}$

interphase demonstrates outstanding electrochemical performance in the half-cell tests, allowing for stable cycling for more than 600 hours (20 mA cm^{-2}, 20 mA h cm^{-2}) with a nucleation overpotential of 72 mV and 800 hours at a high ZUR of 91.5% with a nucleation overpotential of 43 mV. This performance is significantly enhanced, compared to the $SnO_{1.92}$ counterpart, which deposits Zn overlying the artificial interphase (*i.e.*, $SnO_{1.92}$) along the (002) facet. The $SnO_{1.92}$-modified anode sustained cycling for only 140 hours (at 20 mA h cm^{-2}) with an overpotential of 124 mV and 350 hours (a high ZUR of 91.5%) with a polarization voltage of 68 mV. The sulfur cathode, MnO_2 cathode, and $ZnMn_2O_4$ cathode were selected to pair with (i) commercial Zn foil (40 μm) for the full-cell performance evaluation under high plating/stripping, (ii) ultrathin Zn foil (2.8 μm) at low N/P ratios, and (iii) Cu foil under anode-free conditions. The anode modified with the $SnO_{1.17}$ interphase demonstrated capacity retention values of 95.2% and 77.4% when paired with PEDOT@S and MnO_2 cathodes after 600 and 400 cycles, respectively. Noteworthily, in an anode-free system, the anode modified with the $SnO_{1.17}$ interphase retained capacity as high as 81.6%, compared to its original capacity after 200 cycles in a configuration of $ZnMn_2O_4$||$SnO_{1.17}$@Cu, which far surpasses 30.9% for the $ZnMn_2O_4$||$SnO_{1.92}$@Cu cell after 200 cycles.

Results and discussion

X-ray photoelectron spectroscopy (XPS) surveys (Fig. S2, ESI†) with binding energies (BE) ranging from 0 to 900 eV show similar spectra to each other, in which Sn 3d and O 1s peaks are observed with other Sn-related peaks from Sn 3s, 3p, 4s, and 4d excitations. High-resolution XPS (HR-XPS) investigations were performed to analyze the elemental compositions and the valence state of major elements in both $SnO_{1.92}$ and $SnO_{1.17}$ artificial interphases. $SnO_{1.17}$ exhibits two major spin–orbit split pairs of Sn $3d_{5/2}$ at 486.0 eV and Sn $3d_{3/2}$ at 494.4 eV, resulting from the Sn^{2+} state in SnO (Fig. 2(b)). In contrast, the overall peak location of Sn 3d in $SnO_{1.92}$ shifted toward higher binding energy by approximately 0.8 eV, which is attributed to Sn^{4+} in SnO_2.[38] Moreover, the main peak of O 1s in $SnO_{1.92}$ is located at higher binding energies ($\Delta B_E \sim 1.6$ eV) compared to that in $SnO_{1.17}$ (Fig. S3, ESI†), suggesting a higher oxidation state. The Sn to O elemental ratios of the two distinct tin oxide films are estimated to be 1 : 1.92 for the higher oxygen species ($SnO_{1.92}$) and 1 : 1.17 for the lower oxygen phase ($SnO_{1.17}$), respectively through peak area analysis of the HR XPS spectra, indicating slight non-stoichiometric compositions of both phases.

Digital photographs show that the pristine Zn foil turns from shiny silvery to blueish-grey and to pale gold after applying $SnO_{1.92}$ and $SnO_{1.17}$ interphases, respectively (the inset of Fig. 2(c)). Homogeneous films were achieved over a large area (12 × 5.5 cm) for both $SnO_{1.92}$@Zn and $SnO_{1.17}$@Zn samples, suggesting the viability of mass production for practical applications. The X-ray diffraction (XRD) spectra show that the two modified Zn samples ($SnO_{1.92}$@Zn and $SnO_{1.17}$@Zn) well preserve typical metallic Zn, compared to pristine Zn as illustrated in Fig. S4 (ESI†). Noteworthily, two crystalline peaks at the diffraction angles of near 18.1 and 33.4° are observed for $SnO_{1.17}$@Zn (Fig. 2(c) and Fig. S4, ESI†), which correspond to the (001) and (110) planes of the SnO crystal structure (JCPDS no. 06-0395).[39] In contrast, no significant diffraction peaks are observed for $SnO_{1.92}$@Zn, suggesting the amorphous state of the $SnO_{1.92}$ interphase.

To understand the mechanism of crystallinity of Sn–O compounds with different stoichiometries, the chemical potential of the Sn–O system was investigated. The growth conditions of the crystalline phases of SnO and SnO_2 of each element should satisfy the following thermodynamic conditions (eqn (1) and (2)).

$$\Delta\mu_{Sn} + \Delta\mu_0 = \Delta H_{f,SnO} = -2.827 \text{ eV} \quad (1)$$

$$\Delta\mu_{Sn} + 2\Delta\mu_0 = \Delta H_{f,SnO_2} = -4.923 \text{ eV} \quad (2)$$

where $\Delta H_{f,SnO}$ and $\Delta H_{f,SnO_2}$ represent the formation enthalpies of SnO and SnO_2 calculated for bulk Sn and molecular O_2. The crystalline phases of SnO and SnO_2 will be formed when the chemical potential of Sn and O lies within the blue and red regions, respectively in Fig. 2(d). The chemical potentials of Sn and O for the synthesis of Sn–O phases in our experiment are calculated based on ideal gas assumption and marked as a grey dot for SnO ($\Delta\mu_0 = -0.509$ eV, $\Delta\mu_{Sn} = -1.914$) and a yellow dot for SnO_2 ($\Delta\mu_0 = -0.522$ eV, $\Delta\mu_{Sn} = -1.909$ eV) in Fig. 2(d), which are located near each other and closer to the blue line (*i.e.*, crystallization of SnO).[40,41] This comparison suggests that lower energy (*i.e.*, annealing in this study) is required to achieve the crystalline structure of SnO compared to the crystalline structure of SnO_2, leading to the formation of crystalline $SnO_{1.17}$, while $SnO_{1.92}$ remains amorphous. In addition, nanoindentation measurements reveal that the Young's moduli of $SnO_{1.17}$@Zn and $SnO_{1.92}$@Zn are determined to be ~152 GPa and ~207 GPa, both exceeding the ~95 GPa of pristine Zn as indicated in Fig. S5 (ESI†). This enhanced mechanical strength is expected to effectively restrain Zn dendrite formation. Furthermore, the elastic deformation energy densities (U_e) of $SnO_{1.17}$@Zn and $SnO_{1.92}$@Zn, representing the amount of mechanical energy sustained per unit volume when a material undergoes elastic deformation, were calculated to be 1.87 J cm^{-3} and 2.32 J cm^{-3}, respectively (Table S3, ESI†), which are higher than 0.64 J cm^{-3} for pristine Zn. The higher U_e of the artificial interphase enables effective sustainment of substantial volume variations in the anode during Zn^{2+} plating/stripping, thereby enhancing structural stability.[42] Scanning electron microscopy (SEM) and transmission electron microscopy (TEM) analyses were carried out to investigate the characteristics of surface structures of $SnO_{1.17}$ and $SnO_{1.92}$ interphases. The SEM images in Fig. 2(e) and Fig. S6 (ESI†) show the shallow flexures originating from the Zn foil of both $SnO_{1.17}$@Zn and $SnO_{1.92}$@Zn, suggesting the well-maintained surface morphologies of Zn foil due to the thin thickness (~70 nm) of Sn–O interphases. It should be noted that artificial

interphases less than 100 nm thick (considering the thickness (~100 nm) of the solid electrolyte interphase in lithium-ion batteries) are more practical, given that the theoretically required thickness of the Zn foil for ZIBs is approximately 7.4 μm (Note S1 in the ESI†). Uniform interphase coating and the thickness are verified from TEM micrographs of both $SnO_{1.17}$@Zn and $SnO_{1.92}$@Zn in Fig. 2(f) and Fig. S7a (ESI†). Energy dispersive X-ray (EDX) mapping analysis of the selected regions (marked by a yellow rectangle in Fig. 2(f) and Fig. S7, ESI†) unveils that the $SnO_{1.17}$ and $SnO_{1.92}$ layers compactly and uniformly cover the Zn surface as shown in Fig. 2(g) and Fig. S7b (ESI†). The contact angle was tested to evaluate the hydrophobicity of the Sn–O compound layers. $SnO_{1.17}$ and $SnO_{1.92}$ exhibit a higher hydrophobicity as confirmed by larger contact angle values (116.5° and 108.6°) than that of pristine Zn (91.3°) as indicated in Fig. S8 (ESI†), which may be attributed to the lower surface energy of oxide compounds compared to pure metal.[43,44] The strong hydrophobicity of Sn–O compound interphases enables the isolation of the active Zn from the bulk electrolyte, thereby inhibiting water-induced erosion.

Linear sweep voltammetry (LSV) at 5 mV s^{-1} in 2 M Na_2SO_4 aqueous electrolyte based on a three-electrode system was employed to characterize the polarization behaviors of pristine and modified Zn anodes to evaluate the efficacy of the stoichiometrically different Sn–O interphases in HER inhibition. The Zn foil, Pt foil, and Ag/AgCl acted as the working electrode, the counter electrode, and the reference electrode, respectively. Without the Zn^{2+} deposition, the current responses in LSV directly account for HER. The presence of Sn–O compounds decreases the cathodic current density and shifts the potential of the HER at −2 mA cm^{-2} from −1.30 V on pristine Zn to −1.57 V on $SnO_{1.92}$@Zn and −1.78 V on $SnO_{1.17}$@Zn (*vs.* Ag/AgCl) as indicated by the dashed lines in Fig. 3(a). This confirms the stronger resistance of $SnO_{1.17}$ to the HER. Cyclic voltammetry (CV) was used to verify the compatibility and effect of the Sn–O interphase on the electrochemical deposition of

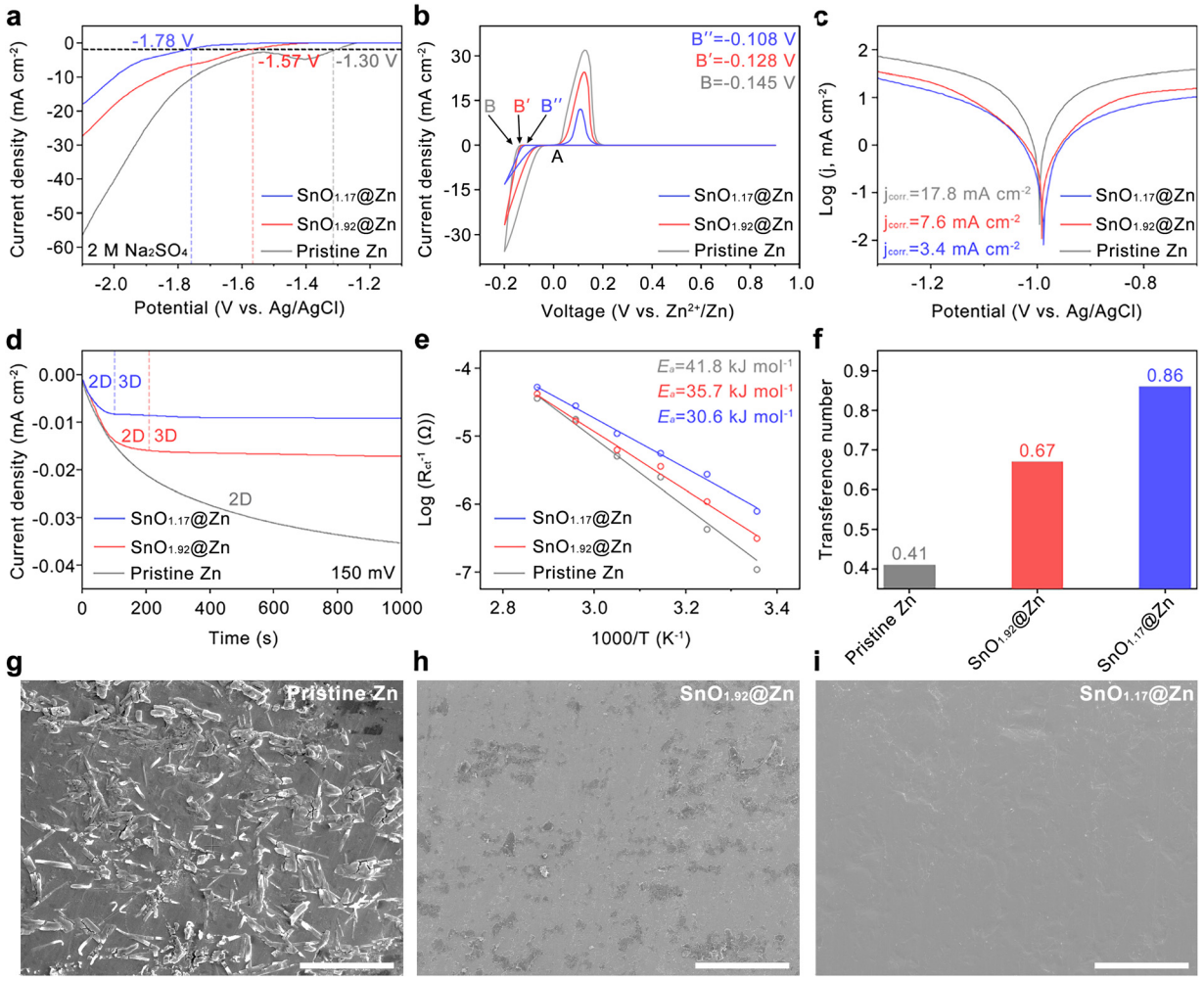

Fig. 3 Effects of the Sn–O interphase on water erosion and kinetics of Zn^{2+} plating/stripping. (a) HER polarization curves of pristine Zn, $SnO_{1.92}$@Zn, and $SnO_{1.17}$@Zn in 2 M Na_2SO_4 aqueous electrolyte at 5 mV s^{-1}. (b) CV of Zn nucleation on pristine Zn, $SnO_{1.92}$@Zn, and $SnO_{1.17}$@Zn at the scan rate of 10 mV s^{-1}. (c) Tafel plots of pristine Zn, $SnO_{1.92}$@Zn, and $SnO_{1.17}$@Zn. (d) Chronoamperograms of pristine Zn, $SnO_{1.92}$@Zn, and $SnO_{1.17}$@Zn anodes. (e) Arrhenius curves of pristine Zn, $SnO_{1.92}$@Zn, and $SnO_{1.92}$@Zn anodes. (f) Zn^{2+} transference numbers of pristine Zn, $SnO_{1.92}$@Zn, and $SnO_{1.17}$@Zn. SEM images of (g) pristine Zn, (h) $SnO_{1.92}$@Zn, and (i) $SnO_{1.17}$@Zn anodes soaked in 2 M $ZnSO_4$ aqueous electrolyte for 5 days (scale bar, 20 μm).

Zn^{2+}. As shown in Fig. 3(b), the oxidation and reduction peaks of Zn||Ti cells appear only when Zn^{2+} stripping/plating occurs, which suggests the electrochemical activity of Zn^{2+} through the Sn–O interphase. The reduction potential increased from B (pristine) to B′ (with $SnO_{1.92}$) and B″ (with $SnO_{1.17}$), signifying that $SnO_{1.17}$ has a better ability to enable the rapid transfer of Zn^{2+} and to alleviate the concentration polarization during Zn^{2+} plating. The higher current densities observed in the $SnO_{1.92}$@Zn and pristine Zn anodes are attributed to parasitic reactions, such as the HER and corrosion, which contribute to the overall reaction current densities.[24,45] Tafel plots in Fig. 3(c) confirm a decreased corrosion current of 3.4 mA cm^{-2} on $SnO_{1.17}$@Zn, which is much lower than that of pristine Zn (17.8 mA cm^{-2}) and $SnO_{1.92}$@Zn (7.6 mA cm^{-2}). These results demonstrate that the $SnO_{1.17}$ interphase shows a stronger resistance to the HER and Zn corrosion than $SnO_{1.92}$. The chronoamperometry (CA) investigations in Fig. 3(d) provide insights into the Zn^{2+} plating mechanisms of the pristine and modified anodes. The current density with the pristine Zn continuously increases, suggesting a long rampant 2D Zn diffusion process, during which Zn^{2+} tends to accumulate at the tip of the Zn anode and generate dendrites.[46,47] In contrast, the current reaches a steady state after about 100 s for $SnO_{1.17}$@Zn and 200 s for $SnO_{1.92}$@Zn, which indicates that the Zn^{2+} diffusion shifts to stable 3D diffusion after a short 2D diffusion, resulting in dense Zn nucleation sites and smooth deposition morphology. This result suggests that the $SnO_{1.17}$ interphase establishes the rapid stabilization of the Zn^{2+} diffusion process more effectively than $SnO_{1.92}$. In addition, the activation energy (E_a) for charge transfer resistance (R_{ct}) estimated from the Arrhenius equation (Fig. 2(e) and Fig. S9, ESI†) allows for the identification of the de-solvation capability of each electrode. Notably, $SnO_{1.17}$@Zn exhibits a significantly lower E_a of 30.6 kJ mol^{-1} compared to 41.8 kJ mol^{-1} for pristine Zn and 35.7 kJ mol^{-1} for $SnO_{1.92}$@Zn. These results indicate that the de-solvation process of Zn^{2+} is more facile on $SnO_{1.17}$ than on $SnO_{1.92}$ and pristine Zn, resulting in improved kinetic conditions. The Zn^{2+} transference number ($t_{Zn^{2+}}$) is measured to evaluate the Zn^{2+} diffusion ability of the Sn–O interphase (Fig. 3(f)). Based on the CA and electrochemical impedance spectroscopy (EIS) tests (Fig. S10, ESI†), $SnO_{1.17}$@Zn exhibits a $t_{Zn^{2+}}$ of 0.86 in Fig. 3(f), which significantly surpasses those of pristine Zn ($t_{Zn^{2+}}$ = 0.41) and $SnO_{1.92}$@Zn ($t_{Zn^{2+}}$ = 0.67), The higher $t_{Zn^{2+}}$ ensures a more efficient transfer of Zn^{2+} while restricting the migration of $SO4^{2-}$ anions, ultimately contributing to uniform Zn^{2+} plating due to the mitigated concentration polarization.[48]

In addition to the contact angle hydrophobicity measurements shown in Fig. S8 (ESI†), the endurance of the $SnO_{1.17}$ interphase to water-induced erosion was further investigated. Pristine Zn, $SnO_{1.92}$@Zn, and $SnO_{1.17}$@Zn anodes were soaked in 2 M $ZnSO_4$ aqueous electrolyte for 5 days. As shown in a SEM microstructure, Fig. 3(g), numerous rod-like products accumulated on the surface of the pristine Zn anode, identified as $Zn_4SO_4(OH)_6{\cdot}5H_2O$ based on XRD results (Fig. S11, ESI†). The formation of $Zn_4SO_4(OH)_6{\cdot}5H_2O$ is known to be induced by the HER on Zn, which elevates the local pH near Zn, thereby triggering the precipitation of by-products.[49] In contrast, minor $Zn_4SO_4(OH)_6{\cdot}5H_2O$ peaks are observed in $SnO_{1.92}$@Zn, while they are entirely absent in $SnO_{1.17}$@Zn as shown in Fig. S11 (ESI†). The SEM microstructure of $SnO_{1.92}$@Zn (Fig. 3(h)) reveals identifiable by-products on the surface, whereas the $SnO_{1.17}$@Zn surface (Fig. 3(i)) remains compact and uniform without any by-products, consistent with the XRD results (Fig. S11, ESI†), suggesting the effective inhibition of water erosion on $SnO_{1.17}$@Zn.

The effect of the $SnO_{1.17}$ and $SnO_{1.92}$ interphases on the electrochemical performance of the Zn anode was investigated using symmetric Zn cells. As shown in Fig. 4(a), the $SnO_{1.17}$@Zn symmetric cell exhibits cycling stability over 3000 h at 1 mA cm^{-2} and 1 mA h cm^{-2} with a much lower overpotential of 33 mV, which is about 2 and 11 times longer lifespan compared to $SnO_{1.92}$@Zn (overpotential: 54 mV) and pristine Zn (overpotential: 58 mV), respectively. Optical images of symmetric cells after cycling demonstrate a significant reduction in HER activity during long-term cycling (>3000 h) due to the presence of the $SnO_{1.17}$ interphase (Fig. S12, ESI†). In addition, at 5 mA cm^{-2} and 5 mA h cm^{-2} (Fig. S13, ESI†), the $SnO_{1.17}$@Zn symmetric cell showed high stability over 1500 h and a lower overpotential of 61 mV, which surpasses the pristine Zn (~190 h, 128 mV) and $SnO_{1.92}$@Zn (~700 h, 92 mV) cells. Additionally, SEM images of the cycled electrodes (Fig. S14, ESI†) show that the $SnO_{1.17}$@Zn electrode maintains a compact and uniform surface, in contrast to the higher roughness and by-products formed on $SnO_{1.92}$@Zn and pristine Zn. These microstructure comparisons suggest that $SnO_{1.17}$, as the anode interface modifier, exhibits a strong capability to restrict the dendrite formation during the Zn^{2+} plating/stripping process. Notably, even at the high current density of 20 mA cm^{-2} with 20 mA h cm^{-2} (Fig. 4(b)), the $SnO_{1.17}$@Zn symmetric cell still sustains stable cycling over 600 h with a relatively low overpotential of 72 mV, which corresponds to a ZUR as high as 85.72%. In contrast, the $SnO_{1.92}$@Zn symmetric cell retained stable cycling only for approximately 140 hours with a larger overpotential of 124 mV, while the pristine Zn cell experienced a short circuit after only about 40 hours. To realize the low N/P ratio for practical applications, an ultrathin Zn (UT Zn) anode with a thickness of around 2.8 μm, which corresponds to an areal capacity of 1.63 mA h cm^{-2}, was made by thermal evaporation. The UT Zn anodes were cycled at 1.5 mA cm^{-2} with 1.5 mA h cm^{-2}, equivalent to a ZUR of ~91.5% as indicated in Fig. S14 (ESI†). The $SnO_{1.17}$@UT Zn symmetric cell stably cycled for 800 h with a low overpotential of 43 mV compared to the ~350 h for the $SnO_{1.92}$@UT Zn (68 mV) and the ~70 h for the pristine UT Zn anodes (76 mV), respectively. This confirms that $SnO_{1.17}$ could promote Zn^{2+} transfer kinetics and enhance cycling stability even at large current densities and high ZURs. Zn||Cu asymmetric cells were adopted to evaluate the Zn^{2+} plating/striping reversibility. The lower nucleation overpotential of $SnO_{1.17}$@Zn at the initial cycle indicates the promoted Zn reaction kinetics (Fig. S16, ESI†). As shown in Fig. 4(c), the $SnO_{1.17}$@Zn cell exhibits a higher

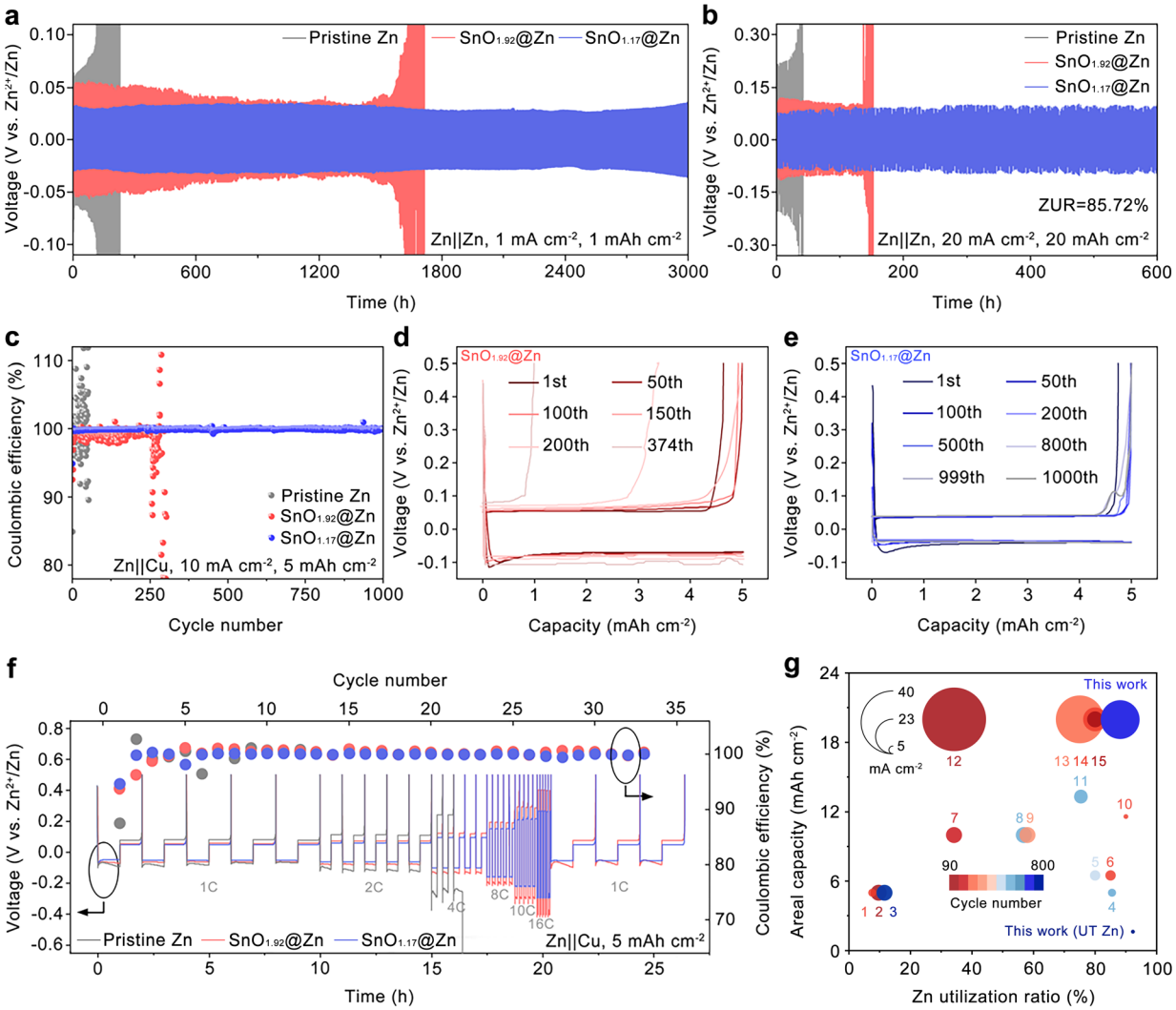

Fig. 4 Electrochemical performance of the Zn||Zn and Zn||Cu half cells. Galvanostatic cycling performance of pristine Zn, $SnO_{1.92}$@Zn, and $SnO_{1.17}$@Zn based on symmetric Zn||Zn cells at (a) 1 mA cm^{-2}, 1 mA h cm^{-2} and (b) 20 mA cm^{-2}, 20 mA h cm^{-2}. (c) Galvanostatic cycling performance of pristine Cu, $SnO_{1.92}$@Cu, and $SnO_{1.17}$@Cu based on asymmetric Zn||Cu cells at 10 mA cm^{-2} and 5 mA h cm^{-2}. Voltage–capacity curves at different cycles of asymmetric Zn||Cu cells with (d) the $SnO_{1.92}$ interphase and (e) the $SnO_{1.17}$ interphase. (f) Rate capacities of asymmetric Zn||Cu cells at an areal capacity of 5 mA h cm^{-2} and current densities from 5 to 80 mA cm^{-2}. (g) Comprehensive comparison of the $SnO_{1.17}$@Zn anode with recently reported Zn anodes.

initial coulombic efficiency (CE) of 96.38% and a higher average CE of 99.87%, compared to the pristine Zn (initial CE: 85.47%, average CE: 90.46%) and $SnO_{1.92}$@Zn (initial CE: 93.52%, average CE: 99.66%). The average CE of 99.87% measured at 5 mA cm^{-2} is comparable to 99.83% obtained at 0.1 mA cm^{-2}, indicating the high reversibility of the $SnO_{1.17}$@Zn anode as indicated in Fig. S17a (ESI†). Additionally, the Aurbach method was employed to eliminate the influence of conversion reactions between Zn metal and the Cu substrate surface, ensuring a more precise determination of the CE. Using this method, the average CE of $SnO_{1.17}$@Zn was determined to be 99.89%, as shown in Fig. S17b (ESI†), further confirming the highly reversible Zn plating/stripping process. The selected voltage profiles of $SnO_{1.92}$@Zn (Fig. 4(d)) show the larger polarization potential between each charge and discharge process compared to those of $SnO_{1.17}$@Zn (Fig. 4(e)), which suggests a facilitated Zn plating process in $SnO_{1.17}$@Zn. Fig. S18 (ESI†) shows that the pristine Zn cell displays unstable cycling behavior after only 50 cycles, with fluctuating voltage profiles attributed to severe water erosion and dendrite growth on the pristine Zn anode. Fig. 4(f) demonstrates the rate capacities of Zn||Cu asymmetric cells. $SnO_{1.17}$@Zn displays a higher average CE of over 99.50% with an areal capacity of 5 mA h cm^{-2} compared to 99.23% for $SnO_{1.92}$@Zn. The pristine Zn cell experienced a short circuit after only 12 cycles, indicating severe non-uniform Zn plating behavior on the surface of bare Zn. These results confirm that the capability of $SnO_{1.17}$ to stabilize the electrodeposition of Zn^{2+} is not limited to low current densities but extended to a much higher density, particularly promising for high-power Zn batteries. Fig. 4(g) presents a comprehensive comparison between this work and reported Zn electrodes with various artificial protection layers in terms of four key parameters (*i.e.*,

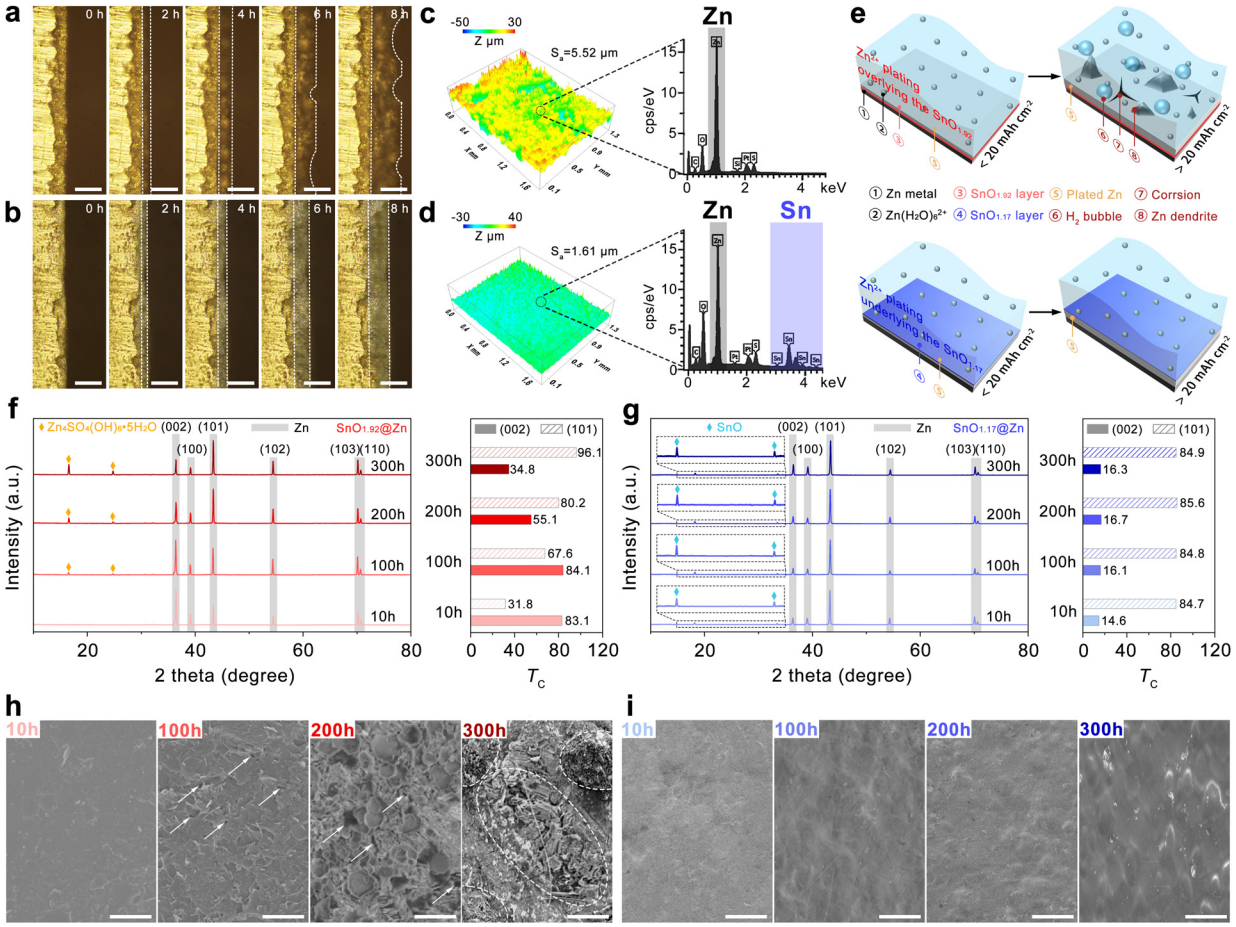

Fig. 5 Comparison of Zn^{2+} plating behavior between $SnO_{1.92}$@Zn and $SnO_{1.17}$@Zn. *In situ* optical microscopy visualization of Zn^{2+} plating on (a) $SnO_{1.92}$@Zn and (b) $SnO_{1.17}$@Zn at 5 mA cm^{-2} (scale bar, 100 μm). Three-dimensional confocal laser microscopy images and EDX analysis of Zn^{2+} plating on (c) $SnO_{1.92}$@Zn and (d) $SnO_{1.17}$@Zn for 8 h. (e) Schematic illustration of the overlying and underlying Zn^{2+} plating of the Sn–O interphase. XRD patterns with the corresponding texture coefficients of (f) $SnO_{1.92}$@UT Zn and (g) $SnO_{1.17}$@UT Zn cycled at 1.5 mA cm^{-2} and 1.5 mA h cm^{-2} for different times. SEM images of (h) $SnO_{1.92}$@UT Zn and (i) $SnO_{1.17}$@UT Zn cycled at 1.5 mA cm^{-2} and 1.5 mA h cm^{-2} for different times (scale bar, 10 μm).

areal capacity, ZUR, cycle number, and current density). Notably, this work leveraging the anti-corrosion ability and favorable Zn^{2+} transfer kinetics of $SnO_{1.17}$ contributed to the significantly extended cycle lives at a 85.7% ZUR for 600 hours at 20 mA cm^{-2} and 20 mA h cm^{-2} as well as at a 91.5% ZUR for 800 hours, outperforming previously reported results with generally less than 500 hours, as indicated in Table S4 (ESI†).

The electrodeposition behavior of Zn^{2+} was characterized to identify the mechanism responsible for the stability difference between $SnO_{1.17}$@Zn and $SnO_{1.92}$@Zn during electrochemical testing. An optical microscopy system was developed to monitor the behavior of substantial Zn^{2+} plating (>20 mA h cm^{-2}) in transparent Zn||Zn cells at a current density of 5 mA cm^{-2} *in situ*. Uneven Zn nucleation sites emerge only after 15 min in pristine Zn and gradually develop into dendritic and Zn protrusions (white circles in Fig. S19, ESI†) on the electrode surface with further plating. In contrast, the *in situ* optical images in Fig. 5(a) ($SnO_{1.92}$@Zn) and 5(b) ($SnO_{1.17}$@Zn) show that the plated Zn (marked with a white dashed line) was uniformly distributed in the initial 4 hours. However, after 4 hours, the Zn^{2+} plating layer in $SnO_{1.92}$@Zn becomes thicker (~48 μm) than the 38 μm-thick layer in $SnO_{1.17}$@Zn. This thickness difference may be attributed to the growth of uneven and random Zn protrusion, resulting in looser Zn^{2+} plating in $SnO_{1.92}$@Zn. Moreover, the thickness of the Zn^{2+} plating layer in $SnO_{1.17}$@Zn is close to the theoretical thickness of Zn^{2+} plating at 5 mA cm^{-2} for 4 hours (~34 μm; Note S1 in the ESI†), suggesting a highly dense Zn^{2+} plating layer formed with $SnO_{1.17}$@Zn. Subsequent Zn^{2+} plating (after 6 hours and 8 hours) in $SnO_{1.92}$@Zn further increased the surface roughness, resulting in the formation of Zn protrusions. In contrast, the $SnO_{1.17}$@Zn interphase layer ensures homogeneous and more compact Zn^{2+} plating throughout the entire 8-hour plating process.

Moreover, the confocal laser microscope was employed to quantitively estimate the topological morphology and roughness of the Zn^{2+} plating layer. Fig. 4(c) and (d) reveal a significant difference in surface roughness (arithmetic mean height, abbreviated as S_a) between $SnO_{1.92}$@Zn and $SnO_{1.17}$@Zn after 8 hours. $SnO_{1.92}$@Zn exhibits a S_a of

5.52 μm, which is more than three times the value of 1.61 μm obtained for $SnO_{1.17}$@Zn, indicating the uneven Zn^{2+} plating at a high Zn^{2+} plating amount (>20 mA h cm^{-2}) in $SnO_{1.92}$@Zn. The surface roughness of pristine Zn after 1 hour Zn plating is 10.02 μm (Fig. S20, ESI†), critically rougher than those of the modified anodes with a longer duration.

Optical photographs in Fig. S21a–c (ESI†) show different colors of the Zn-plated regions of pristine Zn, $SnO_{1.92}$@Zn, and $SnO_{1.17}$@Zn. For the pristine Zn, the apparent color of plated Zn is different from that of pure metallic Zn (initial, not plated). This difference is attributed to the fact that the plated Zn has not undergone polishing, resulting in the absence of metallic shine. Notably, the $SnO_{1.17}$ interphase exhibits a visible transparency of approximately 50%, as demonstrated by the clear visibility of the "Purdue" logo (Fig. S21d and inset, ESI†), which allows the Zn^{2+}-plated region to remain observable even when located underlying the $SnO_{1.17}$-coated glass coverslip. EDX was conducted to further analyze the elemental compositions of coated layers. In the EDX spectrum of $SnO_{1.17}$@Zn (Fig. 5(d)), the characteristic peaks of the element Sn were detected as well as the Zn peaks, whereas no Sn-related peaks were observed in the EDX spectrum of the $SnO_{1.92}$@Zn sample (Fig. 5(c)), confirming the Zn^{2+} plating underlying the $SnO_{1.17}$ interphase, while overlying the $SnO_{1.92}$ interphase of each modification layer. From further analysis of the elemental weight ratio obtained from EDX (Fig. S22 (ESI†)), the ratio of Sn to O in the $SnO_{1.17}$@Zn sample was estimated to be 1 : 1.22, which is close to 1 : 1.17 for the $SnO_{1.17}$ interphase. The slightly higher O content may be attributed to the residual of SO_4^{2-} in the electrolyte and the adsorbed O_2 from the air or detection resolution differences between EDX and XPS. The cross-sectional SEM images and EDX elemental mapping of Sn and Zn for the $SnO_{1.17}$@Zn anode, after Zn^{2+} plating at $\sim$2 mA h cm^{-2}, directly confirm that the plated Zn is located beneath the $SnO_{1.17}$ interphase, as shown in Fig. S23 (ESI†). XRD was employed to further analyze the amorphous/crystalline structure of these Sn–O layers after plating. Two peaks are observed at identical diffraction angles of around 18.1 and 33.4° for plated $SnO_{1.17}$@Zn as shown in Fig. S24 (ESI†), which correspond to SnO(001) and (110) as discussed in Fig. 2(c), further validating Zn plating beneath $SnO_{1.17}$ as shown in Fig. 5(e). The *in situ* observations combined with EDX and XRD also provide strong evidence of both Sn–O interphases controlling the Zn nucleation and growth when the Zn^{2+} plating amount is below 20 mA h cm^{-2} (from 0 to 4 hours). Noteworthily, only the $SnO_{1.17}$ interphase layer can facilitate the formation of a compact and uniform Zn-plated layer from 4 to 8 hours of Zn^{2+} plating (>20 mA h cm^{-2}). Unlike the $SnO_{1.17}$ interphase, the $SnO_{1.92}$ interphase, despite its higher Young's modulus of 207 GPa, does not play any role in suppressing Zn dendrite formation since Zn^{2+} is plated above the $SnO_{1.92}$ interphase. This reveals the limitations of $SnO_{1.92}$ in managing dendrite growth. These results explain the failure process of $SnO_{1.92}$@Zn at a high plating amount with a low ZUR of $\sim$30%.

Furthermore, $SnO_{1.17}$@UT Zn and $SnO_{1.92}$@UT Zn anodes in symmetric Zn||Zn cells at different cycling times were characterized by XRD (Fig. 5(f) and (g)), with aim of understanding the failure mechanism of the $SnO_{1.92}$@UT Zn anode at a high ZUR of 91.5% with a low Zn plating amount of 1.5 mA h cm^{-2} presented earlier in Fig. S15 (ESI†). Peaks at 36.3, 38.9, 43.2, 54.3, 70.1, and 70.7° are observed for both $SnO_{1.92}$@Zn and $SnO_{1.17}$@Zn, which are attributed to the plated Zn. The relative texture coefficient of each plane (T_c, Note 2 in ESI†), representing the preferential growth of a particular plane, was calculated to quantify the phase evolution of the plated Zn. As shown in the right of Fig. 5(f) for $SnO_{1.92}$@Zn, the T_c of the Zn (002) plane at 10 and 100 hours is 83.1 and 84.1 respectively, which is higher than 31.8 and 67.6 for the (101) plane. The T_c comparison indicates that a higher amount of (002)-oriented Zn is plated on the $SnO_{1.92}$ interphase during the initial cycling. Note that, however, the still exposed Zn(101) in the electrolyte continuously reacts with water due to its higher reactivity than Zn (002), which aggravated the HER and corrosion reactions, contributing to the accumulation of $Zn_4SO_4(OH)_6{\cdot}5H_2O$ (marked as yellow diamonds in Fig. 5(f)). The accumulation of by-products deactivates the ability of the $SnO_{1.92}$ interphase to induce Zn(002) plating. Subsequently, the T_c of Zn(002) decreased to 55.1 after 200 hours and to even 34.8 after 300 hours, while the T_c of Zn(101) increased to 80.2 and 96.1 after 200 and 300 hours respectively, due to the faster growth rate of Zn(101) than (002). Consequently, the inevitable HER and corrosion reactions with the exposed Zn(101) in $SnO_{1.92}$@Zn lead to anode failure. In contrast, the T_c of Zn(002) and T_c of Zn(101) in $SnO_{1.17}$@Zn in Fig. 5(g) (right) were retained until 300 hours, suggesting a highly reversible Zn^{2+} plating/stripping process at a high ZUR of 91.5%. Noteworthily, the T_c of Zn(101) plated under the $SnO_{1.17}$ interphase is significantly higher than the T_c of Zn(002) in the entire cycling, indicating the Zn^{2+} plating preferentially along the (101) plane. The faster mass (Zn^{2+}) transfer of the Zn(101) plane contributes to a lower overpotential during the Zn^{2+} plating, compared to the (002)-oriented growth of Zn in $SnO_{1.92}$@Zn.

Fig. 5(h) shows the evolution of the surface morphology of $SnO_{1.92}$@Zn at different cycling times. Initially, a smooth and compact surface was preserved, as observed at 10 hours of cycling, where the $SnO_{1.92}$ interphase benefits uniform Zn^{2+} plating and inhibits the parasitic reactions within the initial 10 hours. However, it is noticed that the surface roughness increased at 100 hours of cycles with several pores (marked with white arrows) generated, which may reduce the compactness of the Zn^{2+} plating layer and lead to the penetration of the water, triggering the mechanical failure and the water corrosion of $SnO_{1.92}$@Zn. As the cycling further proceeded for 200 hours, the roughness of the surface regions of $SnO_{1.92}$@Zn increased drastically with the protrusions and cavities (marked with white arrows). Besides, the pore size increased from hundreds of nanometers to several micrometers, which would lead to a more severe HER and corrosion reaction, which was further confirmed by the SEM image of $SnO_{1.92}$@Zn cycled for 300 hours. A lot of by-products (marked with white dashed lines) derived from the water corrosion process can be identified, resulting in the rapid failure of electrochemical

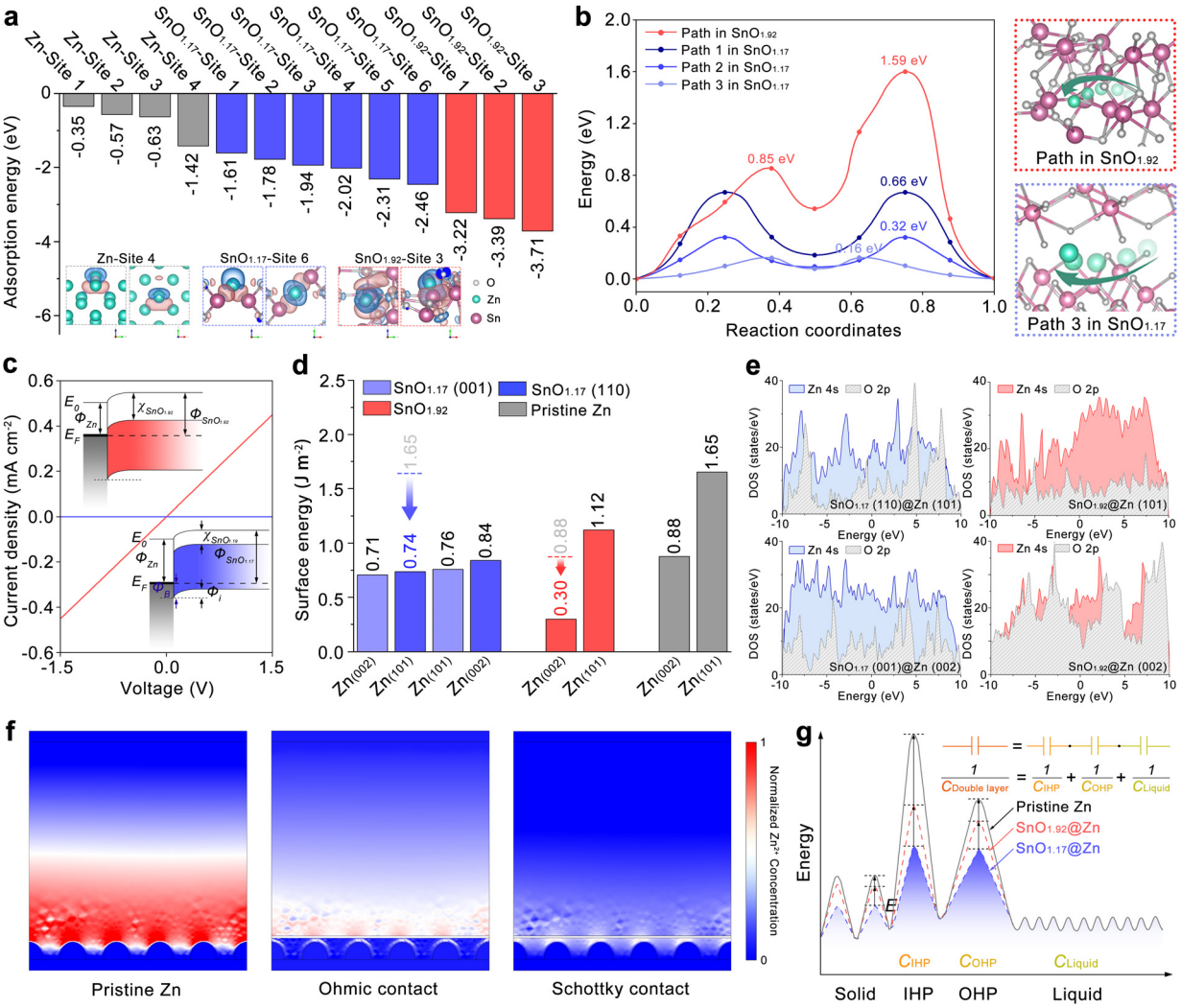

Fig. 6 Mechanistic understanding of the effect of $SnO_{1.17}$ and $SnO_{1.92}$ interphases on Zn^{2+} plating. (a) Adsorption energy of the Zn atoms on Zn, $SnO_{1.17}$, and $SnO_{1.92}$. Insets show the charge density differences of Zn-site 4, $SnO_{1.17}$-site 6, and $SnO_{1.92}$-site 3. (b) MEPs (right) obtained from NEB calculations and the corresponding diffusion energy barrier (left) for Zn^{2+} diffusion through $SnO_{1.92}$ and $SnO_{1.17}$. (c) *I*–*V* curves of $SnO_{1.92}$@Zn (red) and $SnO_{1.17}$@Zn (blue). Insets show schematic illustration of the band diagrams of $SnO_{1.92}$/Zn (top) and $SnO_{1.17}$/Zn (bottom). (d) Surface energies of Zn(002) and Zn(101) with $SnO_{1.17}$ and $SnO_{1.92}$ interphases. (e) The pDOS of Zn 4s and O 2p orbitals of $SnO_{1.17}$@Zn and $SnO_{1.92}$@Zn. (f) Simulated results of Zn^{2+} concentration of pristine Zn, Ohmic contact of $SnO_{1.92}$@Zn, and Schottky contact of $SnO_{1.17}$@Zn. (g) Schematic of the correlation between the energy barrier of Zn^{2+} and the specific diffusion in the OHP, IHP, and solid phase of pristine Zn, $SnO_{1.92}$@Zn, and $SnO_{1.17}$@Zn.

performance. In contrast, the surface morphology of $SnO_{1.17}$@Zn remained compact and smooth throughout the entire process. The (101)-oriented Zn plated underlying $SnO_{1.17}$ was shielded from direct exposure to water molecules by the $SnO_{1.17}$ interphase, protecting it from corrosion and the HER, resulting in a fast and reversible Zn^{2+} plating/stripping process.

Additionally, a combination of experimental and theoretical methods was employed to further understand the Zn^{2+} plating behaviors (position and crystalline orientation) as a function of Sn–O phases. According to the widely accepted ion deposition mechanism, the Zn^{2+} plating process is generally understood to involve three steps: Zn^{2+} adsorption, Zn^{2+} diffusion, and Zn^{2+} reduction.[50] Density functional theory (DFT) was employed to evaluate the adsorption capabilities of the Zn atom by calculating the selected sites on pristine Zn, $SnO_{1.17}$, and $SnO_{1.92}$ as shown in Fig. S25 and Table S5 (ESI†).

As indicated in Fig. 6(a), the Zn atom tends to adsorb on the hollow site on the (101) plane (site 4) with the lowest adsorption energy of −1.42 eV in pristine Zn. For $SnO_{1.17}$, the Zn atom thermodynamically prefers adsorption on the hollow site between two O atoms on the (101) plane (site 6) owing to the lower energy of −2.48 eV. $SnO_{1.92}$ shows an overall stronger adsorption tendency (−3.22 to −3.71 eV) towards the Zn atom with the most preferable Zn adsorption on top of the O atom (site 3; −3.71 eV). The insets show the charge density difference of Zn-site 4, $SnO_{1.17}$-site 6, and $SnO_{1.92}$-site 3. Among the three anode systems, Zn metal shows the least tendency to adsorb Zn

ions (−1.42 eV), which is accounted for by the weakest (the smallest size of the charge difference density region) charge accumulation (red) and depletion (blue) between the Zn and Zn atoms. In $SnO_{1.17}$-site 6 and $SnO_{1.92}$-site 3, the electrons are strongly depleted around the Zn atom, while electrons accumulate around the O adjunct of the Zn atom, suggesting a strong tendency of the Zn atom to donate electrons. Noteworthily, the charge accumulation and depletion regions in $SnO_{1.92}$-site 3 are more prominent than those in $SnO_{1.17}$-site 6, resulting in stronger adsorption. It should be noted that strong adsorption may reduce the Zn nucleation overpotential and improve the uniform Zn deposition but may not lead to the facilitated Zn transport on the anode surface. However, weak adsorption is not beneficial for promoting uniform nucleation and deposition but is always accompanied by a low migration energy barrier, which can achieve fast Zn transport. $SnO_{1.17}$ with moderate adsorption capabilities may achieve an optimization between the Zn nucleation overpotential and Zn transport kinetics compared to metallic Zn and the one with the $SnO_{1.92}$ interphase. An optimal Zn^{2+} adsorption strength of $SnO_{1.17}$ secures both uniform Zn^{2+} plating and fast ion transport on the anode, as proved by electrochemical analysis in Fig. 3 and 4.

The migration energy barriers for Zn^{2+} near the most stable adsorption sites of $SnO_{1.17}$ and $SnO_{1.92}$ were calculated using the climbing image nudged elastic band (NEB) method.[51,52] Fig. 6(b) shows that the migration energy barrier of Zn^{2+} in $SnO_{1.92}$ is about 1.59 eV, and this high energy barrier indicates a slow transport of Zn^{2+}, leading to the sluggish Zn^{2+} plating/stripping behavior. However, Zn^{2+} is able to more easily migrate along the (110) and (001) planes of $SnO_{1.17}$ due to the significantly lower energy barriers of 0.66 and 0.32 eV. The Zn^{2+} migration along the interface of the (110) and (001) planes needs to be considered as well due to the fast kinetics of Zn^{2+}.[53] It should be noted that the grain boundary between (101) and (001) planes (path 3 in $SnO_{1.17}$) is identified to be the fastest Zn^{2+} transport path with the lowest barrier energy of 0.16 eV. Fig. 6(b) and Fig. S26 (ESI†) illustrate the minimum energy path (MEP) of Zn^{2+} connecting the initial and final states of $SnO_{1.17}$ and $SnO_{1.92}$. $SnO_{1.92}$ shows a much narrower Zn^{2+} transport channel with an average distance of 1.62 Å between Zn and O, which contributes to stronger Zn–O interactions and a resultant higher migration energy barrier, compared to 1.78 Å for path 1, 1.91 Å for path 2, and 2.23 Å for path 3 in $SnO_{1.17}$. Additionally, the MEP of $SnO_{1.92}$ that involves seven O atoms experiences more interactions between Zn and O during the Zn^{2+} migration, which hence results in slow Zn^{2+} transport. In contrast, $SnO_{1.17}$ engaging less O atoms (four in path 1, six in path 2, and five in path 3) facilitates the Zn^{2+} migration with a higher ionic conductivity of 1.36×10^{-4} mS cm^{-1}, compared to 8.72×10^{-7} mS cm^{-1} for $SnO_{1.92}$, as measured in Fig. S27 (ESI†). Consequently, excessively strong adsorption and a large migration energy barrier of $SnO_{1.92}$ may impede the diffusion of Zn^{2+} into the bulk Zn. However, $SnO_{1.17}$ is considered to be more suitable for Zn^{2+} diffusion due to the favorable kinetics, which is a prerequisite for Zn^{2+} plating underlying the $SnO_{1.17}$ interphase.

The electrostatic interaction between the Sn–O interphase and the Zn foil was investigated to unveil the effect of Sn–O interphases on the inner Helmholtz plane (IHP), which is crucial for determining the morphology of Zn plating and parasitic reactions. Current–voltage (*I–V*) behaviors of the symmetric cells of Zn|$SnO_{1.17}$|Zn and Zn|$SnO_{1.92}$|Zn (without electrolyte) were characterized to verify the electrostatic interactions at the interface between each Sn–O interphase and the Zn metal, and the results are shown in Fig. 6(c). A linear increased *I–V* curve of the $SnO_{1.92}$/Zn contact implies an Ohmic behavior and a continuous electron transfer across the interface within the applied voltage range from −1.5 to 1.5 V, leading to an areal current density higher than 0.4 mA cm^{-2}. In contrast, the absolute value of the current density of Zn|$SnO_{1.17}$|Zn is lower than 5 μA cm^{-2} within −1.5 and 1.5 V, which suggests that electron transport is significantly limited at the $SnO_{1.17}$/Zn interface. Besides, the measured *I–V* characteristic indicates the non-linear behavior at the $SnO_{1.17}$/Zn interface (Fig. S28, ESI†). The different electrostatic behaviors at the interface are attributed to the distinct band alignments at the Sn–O phase-dominated interface and the types of majority carriers. The majority carrier of $SnO_{1.17}$ has been identified as holes (*i.e.*, p-type) with a work function of 5.42 eV, as shown in Fig. S29 (ESI†).[39] $SnO_{1.17}$ forms a Schottky contact with Zn metal (Φ_{Zn}: ∼4.3 eV) with a Schottky energy barrier (Φ_B), which is the required energy for carrier conduction and estimated to be 1.1 eV from the difference between the work functions (*i.e.*, $\Phi_{SnO1.17} - \Phi_{Zn}$). This non-Ohmic contact would create a charge depletion region in $SnO_{1.17}$ near the interface, limiting the charge carrier transport within the Zn metal during the Zn^{2+} plating/stripping process. Besides, the p-type $SnO_{1.17}$ has a positively charged environment, which delays the electron reception of Zn^{2+} within the $SnO_{1.17}$ interphase until the Zn^{2+} reaches the Zn anode (*i.e.*, at the $SnO_{1.17}$/Zn interface), enabling the Zn^{2+} reduction beneath the $SnO_{1.17}$ interphase.[54] Conversely, electrons work as the majority carriers (*i.e.*, n-type) in $SnO_{1.92}$ with a work function of 4.53 eV.[55] The contact of $SnO_{1.92}$ and Zn metal could facilitate electron transfer since there is no energy barrier for electron flow between $SnO_{1.92}$ and Zn metal, which induces electron accumulation at the surface of $SnO_{1.92}$ in the Zn^{2+} plating process. The electrostatic interaction between Sn and O interphases and Cu foil was also tested to understand the origin of the compelling performance of the $SnO_{1.17}$@Cu anode in Zn||Cu asymmetric cells (Fig. S30, ESI†). Similar to the contacts with Zn, Schottky behavior was also observed when $SnO_{1.17}$ was in contact with Cu metal, while Ohmic behavior occurred in $SnO_{1.92}$ with Cu metal. Consequently, charge carrier transport is restricted to the Cu metal in $SnO_{1.17}$@Cu during Zn^{2+} stripping/plating, by which the reduction location for Zn^{2+} was altered underlying the $SnO_{1.17}$ interphase. However, the electron transfer at the $SnO_{1.92}$/Cu interface was facilitated by the Ohmic contact.

The capacitance of the non-faradaic electric double layer (EDL) was measured *via* alternating current (AC) voltammetry to quantify the effect of $SnO_{1.17}$ and $SnO_{1.92}$ on the ion distribution in IHP. The voltage range of the non-faradaic

region was identified as 0.6–0.9 V (*vs.* Zn^{2+}/Zn) according to the CV measurement (Fig. S31, ESI†). As shown in Fig. S32 (ESI†), the capacitance value of 7.23 μF of the cell with $SnO_{1.17}$ is lower than 12.32 μF for the cell with $SnO_{1.92}$ and 14.42 μF for the pristine sample, which was ascribed to the weaker EDL with the increased distance between the negatively charged surface and IHP. These results suggest that appropriate band alignment through work function engineering may promote the Zn^{2+} migration within IHP as demonstrated in the modified Zn anode surface, *i.e.*, $SnO_{1.17}$/Zn metal. As a result, the Zn^{2+} migrates through the $SnO_{1.17}$ interphase and is reduced to Zn^0 when receiving electrons from Zn metal, inducing the Zn^{2+} plating beneath $SnO_{1.17}$. In contrast, with the high Zn^{2+} migration barrier for $SnO_{1.92}$ and the sufficient electrons supplied by the Ohmic $SnO_{1.92}$/Zn contact, Zn^{2+} tends to be plated on top of the $SnO_{1.92}$ surface.

To further identify the underlying mechanism of the preferential crystalline orientation of Zn electroplating and morphology regulation by Sn–O interphases, the variation of the surface energy of the (002) and (101) planes before and after integrating with Sn–O interphases has been calculated (Fig. 6(d)). The Zn(101) plane exhibited a high surface energy of 1.65 J m^{-2} due to the presence of Zn dangling bonds at the surface, making it challenging to achieve well-aligned Zn(101) plating. The surface energy of the Zn(101) plane decreased from 1.65 J m^{-2} (in pristine Zn) to 0.74 J m^{-2} when the $SnO_{1.17}$ interphase was applied, resulting in reduced Zn(101) nucleation resistance. Even the Zn(002) and (101) planes have similar surface energy after applying the $SnO_{1.17}$ interphase; the Zn(101) plane will cover the (002) plane due to the faster growth rate, leading to the high ratio of the well-aligned Zn (101) plane. The $SnO_{1.92}$ interphase drastically reduces the surface energy of Zn(002) from 0.88 J m^{-2} (in pristine Zn) to 0.30 J m^{-2}, promoting the preferential growth of the Zn(002) plane. The projected density of states (pDOS) was calculated to elucidate why $SnO_{1.17}$ and $SnO_{1.92}$ have different effects on reducing surface energy. As shown in Fig. 6(e), $SnO_{1.17}$ exhibits strong affinity towards the Zn atoms of the (101) plane due to the obvious overlap between the O 2p orbital and the Zn 4s orbital, while only weak pDOS overlap between Zn 4s of the (002) plane and O 2p. In contrast, a strong pDOS overlap between Zn 4s of the Zn (002) plane and O 2p is observed when the $SnO_{1.92}$ interphase is applied, as illustrated in Fig. 6(e), indicating a prominent interaction between $SnO_{1.92}$ and the Zn(002) plane. Besides, only faint pDOS overlaps were observed between O 2p and Zn 4s of Zn(101), suggesting a much weaker interaction between $SnO_{1.92}$ and the Zn(101) plane. In summary, the $SnO_{1.17}$ interphase could saturate the Zn dangling bonds on the surface of Zn(101), resulting in the formation of dative bonds, thus significantly reducing the surface energy of the Zn(101) plane and hence leading to the preferential growth of Zn(101). However, the $SnO_{1.92}$ interphase decreased the surface energy of Zn(002) by strong interactions between O and Zn atoms of the (002) plane, facilitating the growth of (002) orientation.

Finite element analysis was carried out to visualize the concentration distribution of Zn^{2+} in cells with pristine Zn, $SnO_{1.92}$@Zn, and $SnO_{1.17}$@Zn at 0.5 V. As illustrated in Fig. 6(f), pristine Zn exhibited the highest Zn^{2+} concentration gradient, compared to the $SnO_{1.92}$@Zn and $SnO_{1.17}$@Zn, which was ascribed to the high electric field region on the tip of Zn metal as shown in Fig. S34 (ESI†). In the case of $SnO_{1.92}$@Zn and $SnO_{1.17}$@Zn, Ohmic and Schottky contact was built to reflect the charge carrier transmission and inhibition characteristics at the interface between the Sn–O interphase and Zn metal. The $SnO_{1.92}$@Zn exhibits a higher Zn^{2+} concentration gradient above the $SnO_{1.92}$ interphase compared to that above the $SnO_{1.17}$ interphase in $SnO_{1.17}$@Zn, corresponding to the stronger EDL presented in $SnO_{1.92}$@Zn. The Zn^{2+} concentration of $SnO_{1.92}$@Zn below the Sn–O interphase is drastically decreased due to the limited migration capability of Zn^{2+} in $SnO_{1.92}$. Consequently, Zn^{2+} ions tend to accumulate and undergo reduction by gaining electrons at the surface of the $SnO_{1.92}$ interphase. In contrast, the Zn^{2+} concentration beneath the $SnO_{1.17}$ interphase is similar to that above it, as Zn^{2+} ions easily migrate in $SnO_{1.17}$ with a lower energy barrier (as in Fig. 6(a) and (b)) and are subsequently reduced to (101)-oriented Zn underlying the $SnO_{1.17}$ interphase. As a result, $SnO_{1.17}$@Zn facilitates rapid Zn^{2+} diffusion with a lower energy barrier (liquid–solid) and the faster growth rate of Zn (101) plane (solid) as illustrated schematically in Fig. 6(g).

Various cathodes have been adopted to assemble Zn-based full batteries to evaluate the reliability of $SnO_{1.92}$@Zn and $SnO_{1.17}$@Zn for practical applications. The cycling stability of the Zn-based full batteries was tested at low rates because the most stringent proof of stability is not necessarily manifested by the number of cycles but rather by the time the system spends in the fully charged state.[56,57] The sulfur cathode was selected due to its high specific capacity, leading to a higher ZUR than the other commonly used cathode with the same mass loading. The sulfur cathode was manufactured based on the method reported in our previous research.[58] The manufactured PEDOT@S cathodes with a mass loading of around 6 mg cm^{-2} were coupled with commercialized Zn metal anodes (40 μm), contributing to an N/P ratio of 4.6 at 0.5 A g^{-1}. The PEDOT@S||$SnO_{1.17}$@Zn cell demonstrates excellent reversibility and rate capability, retaining over 95.2% of its capacity and exhibiting an R_{ct} of 317 Ω after 600 cycles, as shown in Fig. 7(a) and Fig. S35 (ESI†). This performance surpasses that of the PEDOT@S||$SnO_{1.92}$@Zn battery, which has a capacity retention of 77.4% and an R_{ct} of 487 Ω. The PEDOT@S||Zn battery stably cycled for 334 cycles with a capacity retention of 66.9% and an R_{ct} of 834 Ω before a short circuit occurred at cycle 335 due to the growth of Zn dendrites. The SEM image of pristine Zn after cycling in Fig. S36 (ESI†) exhibits a rough surface with protrusions and cracks, which contributes to the unevenness of Zn^{2+} plating and severe parasite reactions. Several potholes can be observed on the surface of $SnO_{1.92}$@Zn, suggesting the inevitable corrosion reaction due to the direct contact between Zn(101) and water. In contrast, the smooth morphology of $SnO_{1.17}$@Zn after cycling in Fig. S37 (ESI†) indicates superior cycling reversibility. The PEDOT@S||$SnO_{1.17}$@Zn battery delivered higher capacities at various current densities than the

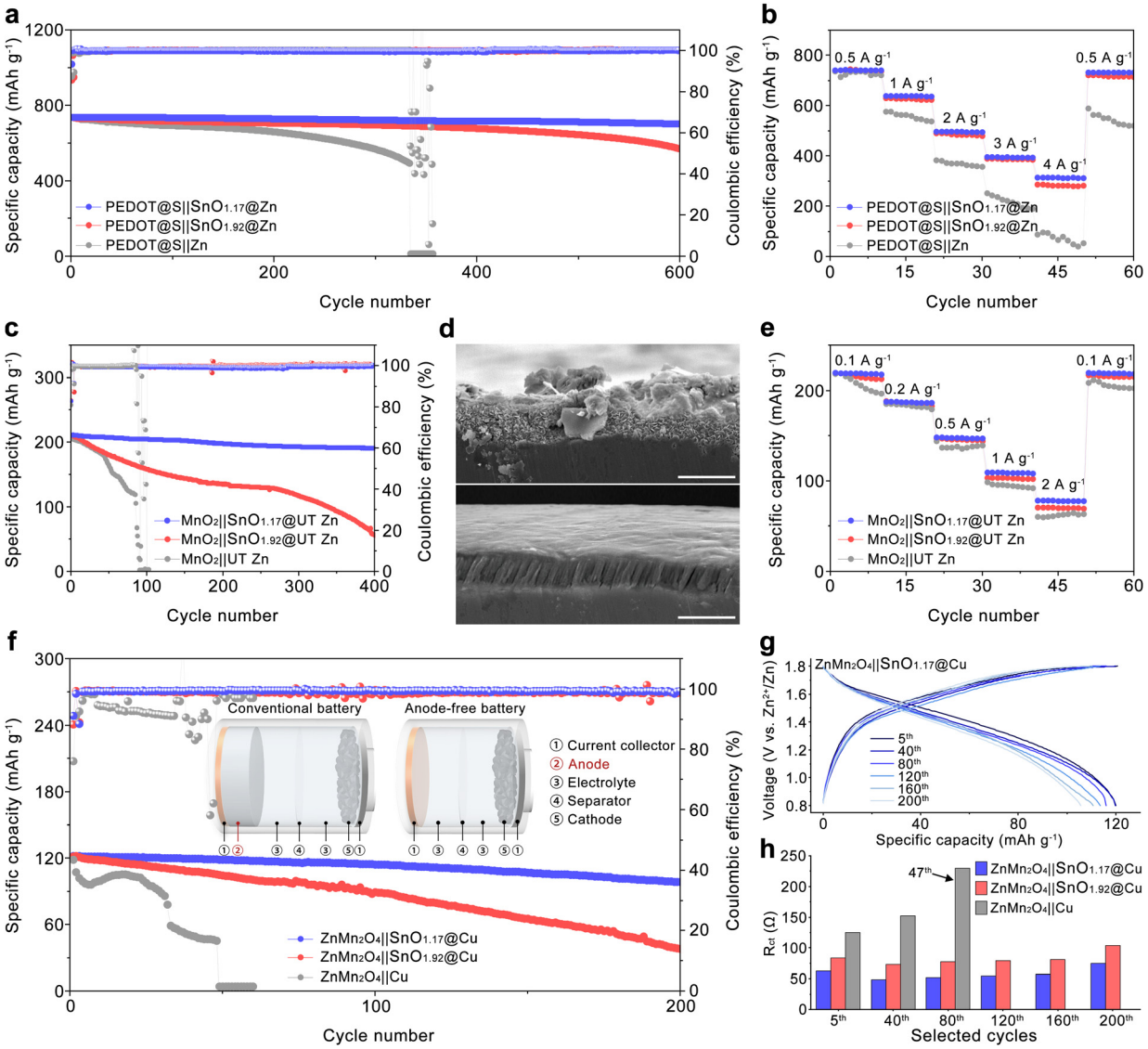

Fig. 7 Electrochemical performance of full batteries. (a) Cycling performance and (b) rate performance of the PEDOT@S||Zn batteries with commercialized Zn foils (40 μm); (c) cycling performance of MnO_2||Zn cells batteries with UT Zn anodes (2.8 μm); (d) cross-sectional SEM images of cycled $SnO_{1.92}$@UT Zn (top) and $SnO_{1.17}$@UT Zn (bottom) (scale bar, 5 μm); (e) rate performance of MnO_2||Zn batteries with UT Zn anodes; (f) cycling performance of anode-free $ZnMn_2O_4$||Cu with pristine Cu, $SnO_{1.92}$@Cu, and $SnO_{1.17}$@Cu. Inset shows the schematic illustration of the conventional Zn-based and anode-free Zn metal batteries. (g) Voltage–capacity curves and (h) charge transfer resistance of the anode-free battery at selected cycles.

PEDOT@S||$SnO_{1.92}$@Zn battery and the PEDOT@S||Zn battery, mainly due to faster mass transfer at the (101) Zn orientation in comparison with that at (002) Zn orientation. Moreover, the charge–discharge profiles at different rates in Fig. S37 (ESI†) revealed that the PEDOT@S||$SnO_{1.17}$@Zn battery show a smaller voltage hysteresis compared with the PEDOT@S||$SnO_{1.92}$@Zn battery and the PEDOT@S||Zn battery, originating from the facilitated Zn^{2+} transfer process at $SnO_{1.17}$@Zn. To further decrease the N/P ratio during the full cell tests, UT Zn (2.8 μm) was employed to pair with the MnO_2 cathode, which delivered 225 mA h g^{-1} when paired with a commercialized Zn anode (40 μm) as shown in Fig. S38 (ESI†), leading to an N/P ratio of 1.26 at a current density of 0.1 A g^{-1}. $MnSO_4$ solution has been added as the electrolyte additive to improve capacity and stability. The MnO_2||UT Zn battery underwent a fast degradation at the initial 84 cycles before experiencing a short circuit, which was caused by the accumulation of by-products and Zn dendrite formation due to the uneven Zn^{2+} plating as identified in Fig. S39 (ESI†). In contrast, the MnO_2||$SnO_{1.17}$@UT Zn battery achieved a capacity retention of 90.5% with an average CE of 99.68% after 400 cycles at 0.1 A g^{-1}, exceeding the capacity retention of 26.4% and an average CE of 98.92% for the MnO_2||$SnO_{1.92}$@UT Zn battery. Moreover, the MnO_2||$SnO_{1.17}$@UT Zn battery demonstrates a lower R_{ct} variation of 21 Ω compared to 30 Ω for the MnO_2||$SnO_{1.92}$@UT Zn battery and 89 Ω for the MnO_2||UT Zn as shown in Fig. S40 (ESI†), respectively. The inferior reversibility of the MnO_2||$SnO_{1.92}$@UT Zn battery is mainly attributed to the accumulation

of the by-products on the surface of the anode as indicated in Fig. 7(d). The $SnO_{1.17}$@UT Zn anode shows a smooth surface and a more compact Zn^{2+} plating layer, verifying the evenness of Zn^{2+} plating behavior and restricted parasite reactions at $SnO_{1.17}$@UT Zn. The MnO_2||$SnO_{1.17}$@UT Zn battery exhibits higher specific capacities of 109.6 and 78.9 mA h g^{-1} at 1 A g^{-1} and 2 A g^{-1} as shown in Fig. 7(e), compared to 102.3 and 69.7 mA h g^{-1} for the MnO_2||$SnO_{1.92}$@UT Zn battery and 97.8 and 59.9 mA h g^{-1} for the MnO_2||UT Zn battery, respectively. This should be related to the favorable Zn^{2+} transfer process at the anode in the MnO_2||$SnO_{1.17}$@UT Zn battery.

As shown in the inset of Fig. 7(f), conventional Zn-based batteries typically use a thick Zn metal foil (100 to 200 μm), leading to a high N/P ratio (60 to 120) within the battery. This not only results in significant material waste but also substantially compromises the energy density at the battery level. However, the configuration of anode-free Zn aqueous batteries represents a promising technique to improve energy density. To achieve the anode-free configuration in the battery, the $ZnMn_2O_4$ cathode was chosen to pair with Cu foil as an anode-free Zn aqueous battery, where $ZnMn_2O_4$ is the sole source of Zn^{2+} during cycling. As shown in Fig. S41 (ESI†), the as-synthesized $ZnMn_2O_4$ cathode materials delivered a specific capacity of around 155 mA h g^{-1} at 0.05 A g^{-1} when paired with conventional Zn foil (40 μm). Then the as-prepared $ZnMn_2O_4$ cathode with a mass loading around 2.2 mg cm^{-2} was coupled with Cu foil, $SnO_{1.92}$@Cu, and $SnO_{1.17}$@Cu, respectively, as anode-free batteries. The $ZnMn_2O_4$||Cu battery rapidly faded within 47 cycles under these extreme test conditions as shown in Fig. 7(f). However, the $ZnMn_2O_4$||$SnO_{1.17}$@Cu battery retained 81.6% of its original capacity after 200 cycles at 0.1 A g^{-1}, which is much higher than 30.9% for the $ZnMn_2O_4$||$SnO_{1.92}$@Cu battery (Fig. 7(f)). Moreover, the $ZnMn_2O_4$||$SnO_{1.17}$@Cu battery shows a lower voltage decay of 0.03 V, compared to the voltage decay of 0.09 V in the $ZnMn_2O_4$||$SnO_{1.92}$@Cu battery as illustrated in Fig. 7(g) and Fig. S42 (ESI†). The resistance evolution during cycling was evaluated by EIS (Fig. S43, ESI†). The R_{ct} value of the $ZnMn_2O_4$||Cu battery drastically increased to 231 Ω at the 47th cycle, which should be ascribed to the accumulation of insulated by-products resulting from the corrosion reactions. In contrast, the R_{ct} value of the $ZnMn_2O_4$||$SnO_{1.17}$@Cu battery remained lower than 80 Ω during the entire cycling process, suggesting the favorable kinetic conditions for Zn^{2+} plating in the $ZnMn_2O_4$||$SnO_{1.17}$@Cu battery. SEM images further confirm the intensive parasitic reactions occurring during the cycling with vast amounts of by-products accumulated on the surface of the Cu foil, leading to the rapid failure of the $ZnMn_2O_4$||Cu battery (Fig. S44, ESI†). There are a lot of micro-caves that can be observed on the surface of $SnO_{1.92}$@Cu, implying the presence of severe HERs during battery cycling. In contrast, $SnO_{1.17}$@Cu shows a flat surface without any accumulation of the by-products due to the regulated Zn^{2+} plating behavior and restricted parasitic reactions, which contributes to the superior cycling performance of the $ZnMn_2O_4$||$SnO_{1.17}$@Cu battery. The successful demonstration of anode-free Zn aqueous batteries verifies the advantages of the $SnO_{1.17}$ interphase in promoting the edge of the energy density of the Zn-based energy storage devices.

Conclusions

In summary, we successfully induce (101)-oriented Zn^{2+} plating while spontaneously passivating the plated Zn(101) using a thin $SnO_{1.17}$ artificial interphase. Further analyses reveal that the electron transfer from the O 2p orbital of the $SnO_{1.17}$ interphase to the Zn 4s orbital of Zn(101) saturated the Zn dangling bonds at Zn(101), thus lowering the nucleation energy barrier of Zn(101) and leading to the preferential growth of Zn(101). The faster Zn^{2+} transfer at Zn(101) and high ionic conductivity of the $SnO_{1.17}$ interphase brought about favorable Zn^{2+} plating/stripping kinetics, resulting in the lower Zn nucleation overpotential and the smaller voltage hysteresis. In addition, the Zn^{2+} plating location of the underlying $SnO_{1.17}$ interphase was determined by synergetic effects of low Zn^{2+} diffusion barriers and electrostatic electron shielding within the $SnO_{1.17}$ interphase, which isolates the plated Zn(101) from water molecules, ensuring high reversibility and rapid Zn^{2+} migration even at elevated ZURs.

Consequently, the $SnO_{1.17}$@Zn symmetric cell operated stably for 600 hours at 20 mA h cm^{-2} with a ZUR of 85.7% and a lower overpotential of 72 mV compared to the 140 hours and the overpotential of 124 mV for $SnO_{1.92}$@Zn. The $SnO_{1.17}$@UT Zn symmetric cell cycled stably for 800 hours with a ZUR of 91.5% and retained 90.5% of its original capacity when paired with an MnO_2 cathode in a full cell under low N/P ratio (1.26) conditions. Moreover, the Cu||Zn asymmetric cell modified with the $SnO_{1.17}$ interphase achieved an average CE of 99.50% at 5 mA cm^{-2} and 5 mA h cm^{-2} for 1000 cycles and demonstrated a high-capacity retention of 81.6% after 200 cycles at a low current density of 0.1 A g^{-1} when applied in an anode-free system. This work outlines the potential of Zn(101) for reversible and kinetically favorable Zn^{2+} plating/stripping to achieve high ZURs at high current densities for practical ZIBs.

Author contributions

Y. Z. and S. L. conceived the idea, designed the experiments, and wrote and revised the manuscript. Y. Z., M. K., F. Q., and D. H. L. performed experiments and formal analysis. C. S. K., J. P. and C. K. conducted related characterization procedures. F. L. helped with the analysis of the electrochemical data. S. L. supervised the project. H.-W. S. and S. L. provided the funding acquisition. All the authors commented on the manuscript.

Data availability

All data that support the findings of this study are available from the corresponding author upon reasonable request.

Conflicts of interest

There are no conflicts to declare.

Acknowledgements

This work was supported by the US National Science Foundation, Award numbers CBET-2207302 and CMMI-2318677. SL and HWS acknowledge the support from the National Research Council of Science & Technology (NST) grant by the Korea Ministry of Science and ICT (MSIT) (CRC23021-000).

Notes and references

1 G. Fang, J. Zhou, A. Pan and S. Liang, *ACS Energy Lett.*, 2018, **3**, 2480–2501.
2 F. Wang, O. Borodin, T. Gao, X. Fan, W. Sun, F. Han, A. Faraone, J. A. Dura, K. Xu and C. Wang, *Nat. Mater.*, 2018, **17**, 543–549.
3 H. Pan, Y. Shao, P. Yan, Y. Cheng, K. S. Han, Z. Nie, C. Wang, J. Yang, X. Li, P. Bhattacharya, K. T. Mueller and J. Liu, *Nat. Energy*, 2016, **1**, 16039.
4 C. Xu, B. Li, H. Du and F. Kang, *Angew. Chem., Int. Ed.*, 2012, **51**, 933–935.
5 H. Li, L. Ma, C. Han, Z. Wang, Z. Liu, Z. Tang and C. Zhi, *Nano Energy*, 2019, **62**, 550–587.
6 Z. Zhao, J. Zhao, Z. Hu, J. Li, J. Li, Y. Zhang, C. Wang and G. Cui, *Energy Environ. Sci.*, 2019, **12**, 1938–1949.
7 Z. Wu, Y. Wang and C. Zhi, *Joule*, 2024, **8**, 2442–2448.
8 L. Ma, M. A. Schroeder, O. Borodin, T. P. Pollard, M. S. Ding, C. Wang and K. Xu, *Nat. Energy*, 2020, **5**, 743–749.
9 M. Zhou, S. Guo, J. Li, X. Luo, Z. Liu, T. Zhang, X. Cao, M. Long, B. Lu, A. Pan, G. Fang, J. Zhou and S. Liang, *Adv. Mater.*, 2021, **33**, 2100187.
10 W. Yuan, X. Nie, G. Ma, M. Liu, Y. Wang, S. Shen and N. Zhang, *Angew. Chem., Int. Ed.*, 2023, **62**, e202218386.
11 G. Liu, Y. Tang, Y. Wei, H. Li, J. Yan, Z. Feng, W. Du, Q. Yang, M. Ye, Y. Zhang, Z. Wen, X. Liu and C. C. Li, *Angew. Chem., Int. Ed.*, 2024, e202407639.
12 P. Curie, *Bull. Mineral.*, 1885, **8**, 145–150.
13 S. F. Li, X. J. Zhao, X. S. Xu, Y. F. Gao and Z. Zhang, *Phys. Rev. Lett.*, 2013, **111**, 115501.
14 S. Chen, K. Ouyang, Y. Liu, M. Cui, G. Pu, Y. Wang, K. Zhang and Y. Huang, *Angew. Chem., Int. Ed.*, 2024, e202409303.
15 X. Zhang, J. Li, Y. Liu, B. Lu, S. Liang and J. Zhou, *Nat. Commun.*, 2024, **15**, 2735.
16 H. Zhang, Y. Zhong, J. Li, Y. Liao, J. Zeng, Y. Shen, L. Yuan, Z. Li and Y. Huang, *Adv. Energy Mater.*, 2023, **13**, 2203254.
17 J. Zheng, Q. Zhao, T. Tang, J. Yin, C. D. Quilty, G. D. Renderos, X. Liu, Y. Deng, L. Wang, D. C. Bock, C. Jaye, D. Zhang, E. S. Takeuchi, K. J. Takeuchi, A. C. Marschilok and L. A. Archer, *Science*, 2019, **366**, 645–648.
18 Y. Wang, X. Xu, J. Yin, G. Huang, T. Guo, Z. Tian, R. Alsaadi, Y. Zhu and H. N. Alshareef, *Adv. Mater.*, 2023, **35**, 2208171.
19 Z. Zhang, Y. Wang, J. Sun, L. Dang, Q. Li, X. He, Z. Liu and Z. Lei, *Small*, 2024, 2402636.
20 R. Yuksel, O. Buyukcakir, W. K. Seong and R. S. Ruoff, *Adv. Energy Mater.*, 2020, **10**, 1904215.
21 X. Zhang, J. Li, K. Qi, Y. Yang, D. Liu, T. Wang, S. Liang, B. Lu, Y. Zhu and J. Zhou, *Adv. Mater.*, 2022, **34**, 2205175.
22 W. Xie, K. Zhu, W. Jiang, H. Yang, M. Ma, L. Zhao and W. Yang, *ACS Nano*, 2024, **18**, 21184–21197.
23 J. Zhang, W. Huang, L. Li, C. Chang, K. Yang, L. Gao and X. Pu, *Adv. Mater.*, 2023, **35**, 2300073.
24 Z. Liu, Z. Guo, L. Fan, C. Zhao, A. Chen, M. Wang, M. Li, X. Lu, J. Zhang, Y. Zhang and N. Zhang, *Adv. Mater.*, 2024, **36**, 2305988.
25 Z. Cheng, K. Wang, J. Fu, F. Mo, P. Lu, J. Gao, D. Ho, B. Li and H. Hu, *Adv. Energy Mater.*, 2024, **14**, 2304003.
26 Y. Zhang, X. Han, R. Liu, Z. Yang, S. Zhang, Y. Zhang, H. Wang, Y. Cao, A. Chen and J. Sun, *Small*, 2022, **18**, 2105978.
27 Y. Su, L. Xu, Y. Sun, W. Guo, X. Yang, Y. Zou, M. Ding, Q. Zhang, C. Qiao, S. Dou, T. Cheng and J. Sun, *Small*, 2024, **20**, 2308209.
28 Y. Wang, C. Chen, A. Xu, J. Lv, M. Huang, T. Ren, J. Bai, H. Wang and X. Liu, *Adv. Energy Mater.*, 2024, 2404071.
29 Q. Ren, X. Tang, Y. Guo, X. Liao, C. Zhang, Z. Zhu, P. Wang, W. Wang, Y. Li, W. Song, S. Wang, K. He, Z.-B. Wang and Y. Yuan, *Adv. Energy Mater.*, 2024, 2403961.
30 K. Wandelt, *Encyclopedia of interfacial chemistry: surface science and electrochemistry*, Elsevier, 2018.
31 R. Zhang, X.-B. Cheng, C.-Z. Zhao, H.-J. Peng, J.-L. Shi, J.-Q. Huang, J. Wang, F. Wei and Q. Zhang, *Adv. Mater.*, 2016, **28**, 2155–2162.
32 J. Yang, B. Yin, Y. Sun, H. Pan, W. Sun, B. Jia, S. Zhang and T. Ma, *Nano-Micro Lett.*, 2022, **14**, 42.
33 S. Higashi, S. W. Lee, J. S. Lee, K. Takechi and Y. Cui, *Nat. Commun.*, 2016, **7**, 11801.
34 R. E. A. Ardhi, G. Liu and J. K. Lee, *ACS Energy Lett.*, 2021, **6**, 1432–1442.
35 R. T. Tung, *Appl. Phys. Rev.*, 2014, **1**, 011304.
36 İ. Taşçıoğlu, U. Aydemir, Ş. Altındal, B. Kınacı and S. Özçelik, *J. Appl. Phys.*, 2011, **109**, 054502.
37 C. Y. Wu, *J. Appl. Phys.*, 1980, **51**, 3786–3789.
38 J. Szuber, G. Czempik, R. Larciprete, D. Koziej and B. Adamowicz, *Thin Solid Films*, 2001, **391**, 198–203.
39 D. H. Lee, H. Park, M. Clevenger, H. Kim, C. S. Kim, M. Liu, G. Kim, H. W. Song, K. No, S. Y. Kim, D.-K. Ko, A. Lucietto, H. Park and S. Lee, *ACS Appl. Mater. Interfaces*, 2021, **13**, 55676–55686.
40 C. Kittel, *Am. J. Phys.*, 1967, **35**, 483–487.
41 R. Baierlein, *Am. J. Phys.*, 2001, **69**, 423–434.
42 Y. Gao, X. Du, Z. Hou, X. Shen, Y.-W. Mai, J.-M. Tarascon and B. Zhang, *Joule*, 2021, **5**, 1860–1872.
43 M. Bajdich, J. K. Nørskov and A. Vojvodic, *Phys. Rev. B: Condens. Matter Mater. Phys.*, 2015, **91**, 155401.
44 A. Feng, B. J. McCoy, Z. A. Munir and D. Cagliostro, *Mater. Sci. Eng., A*, 1998, **242**, 50–56.
45 G. Liu, Y. Tang, Y. Wei, H. Li, J. Yan, Z. Feng, W. Du, Q. Yang, M. Ye, Y. Zhang, Z. Wen, X. Liu and C. C. Li, *Angew. Chem., Int. Ed.*, 2024, **63**, e202407639.
46 J. Feng, X. Li, Y. Ouyang, H. Zhao, N. Li, K. Xi, J. Liang and S. Ding, *Angew. Chem., Int. Ed.*, 2024, e202407194.

47 D. Xie, Z.-W. Wang, Z.-Y. Gu, W.-Y. Diao, F.-Y. Tao, C. Liu, H.-Z. Sun, X.-L. Wu, J.-W. Wang and J.-P. Zhang, *Adv. Funct. Mater.*, 2022, **32**, 2204066.
48 M. Doyle and J. Newman, *J. Electrochem. Soc.*, 1995, **142**, 3465.
49 M. Liu, W. Yuan, G. Ma, K. Qiu, X. Nie, Y. Liu, S. Shen and N. Zhang, *Angew. Chem., Int. Ed.*, 2023, **62**, e202304444.
50 S. Wu, Z. Hu, P. He, L. Ren, J. Huang and J. Luo, *eScience*, 2023, **3**, 100120.
51 G. Henkelman, B. P. Uberuaga and H. Jónsson, *J. Chem. Phys.*, 2000, **113**, 9901–9904.
52 G. Henkelman and H. Jónsson, *J. Chem. Phys.*, 2000, **113**, 9978–9985.
53 L. Wang, B. Zhang, W. Zhou, Z. Zhao, X. Liu, R. Zhao, Z. Sun, H. Li, X. Wang, T. Zhang, H. Jin, W. Li, A. Elzatahry, Y. Hassan, H. J. Fan, D. Zhao and D. Chao, *J. Am. Chem. Soc.*, 2024, **146**, 6199–6208.
54 Z. Sun, F. Bu, Y. Zhang, W. Zhou, X. Li, X. Liu, H. Jin, S. Ding, T. Zhang, L. Wang, H. Li, W. Li, C. Zhang, D. Zhao, Y. Wang and D. Chao, *Angew. Chem., Int. Ed.*, 2024, **63**, e202402987.
55 M. N. Islam and M. O. Hakim, *J. Mater. Sci. Lett.*, 1986, **5**, 63–65.
56 J. C. Burns, G. Jain, A. J. Smith, K. W. Eberman, E. Scott, J. P. Gardner and J. R. Dahn, *J. Electrochem. Soc.*, 2011, **158**, A255.
57 A. J. Smith, J. C. Burns and J. R. Dahn, *Electrochem. Solid-State Lett.*, 2010, **13**, A177.
58 Y. Zhang, H. W. Song, K. R. Crompton, X. Yang, K. Zhao and S. Lee, *Nano Energy*, 2023, **115**, 108756.

